# Chapter 11
# Induction Synchrotron

**Ken Takayama**

The concept of a synchrotron employing induction acceleration devices is described [1]. The concept becomes more clear when one contrasts the *Induction Synchrotron* with an RF synchrotron, which has been employed in all high-energy circular accelerators since being independently invented by McMillan [2] and Veksler [3]. In the Induction Synchrotron, the accelerating devices of a conventional synchrotron, such as an RF cavity, are replaced with induction devices. Acceleration and longitudinal confinement of charged particles are realized with independently driven induction devices. This concept of separated-function longitudinal dynamics brings about a significant freedom of beam handling relative to conventional circular accelerators, typically in which radio-frequency waves in a resonant cavity simultaneously take both roles of acceleration and longitudinal confinement. Associated with this separated-function, various aspects are realized such as the formation of a *superbunch*, which is an extremely long-bunch with a uniform line-density. Newly developed injection/extraction schemes, which make use of unique features of the Induction Synchrotron, are illustrated with the help of computer simulations. Longitudinal beam dynamics are unique as compared with RF synchrotrons. Elementary descriptions of barrier bucket acceleration are given. Transition crossing used to be one of the biggest issues in RF-synchrotrons. We contrast transition crossing in the RF and induction cases. It is found that the induction approach allows considerably more freedom to address issues. Technical details of key components of the induction accelerating cell and the switching power supply driving the cell are given.

## 11.1 Principle of Induction Synchrotron

The Induction Synchrotron employs induction cells for the acceleration and longitudinal confinement of charged particles. The two functions of acceleration and confinement can be independently achieved with induction step-voltages. This aspect

---

K. Takayama (✉)
High Energy Accelerator Research Organization (KEK), Tsukuba 305–0801, Japan
e-mail: takayama@post.kek.jp

K. Takayama, R.J. Briggs (eds.), *Induction Accelerators*, Particle Acceleration and Detection, DOI 10.1007/978-3-642-13917-8_11,

is an essential point why the Induction Synchrotron proposed by Takayama and Kishiro [1] is distinguished from the preceding concepts, such as recirculating LIAs, described in Chap. 2, or an Induction Synchrotron accelerator proposed by Putnam [4]. For the purpose of contrasting novel features of the Induction Synchrotron with the RF synchrotron, we present a brief review of the longitudinal beam dynamics in a conventional RF synchrotron. In the conventional RF synchrotron, the acceleration and longitudinal focusing are realized with radio-frequency waves (RF) in a well-known manner. Figure 11.1 shows the relation between a bunch of charged particles and the RF voltage in time. In the figure we assume that particles in the bunch have positive charge and the particle energy is below the transition energy.

A synchronous particle, which is located at the center of a bunch, is accelerated with a net magnitude of RF voltage, that is, $V_{\mathrm{RF}} \sin \phi_s$, where $V_{\mathrm{RF}}$ is the amplitude of the RF voltage and $\phi_s$ is called the synchronous phase. The energy of a synchronous particle is ramped with the magnetic guiding-fields to synchronously keep the bunch centered in the machine aperture. A particle in the bunch-head is accelerated less with respect to the synchronous particle, and conversely, a particle in the bunch-tail is accelerated more. Thus particles are focused towards the synchronous particle, while losing or gaining energy. All of the particles in the bunch are confined in the longitudinal direction. This focusing is provided by the inherent gradient in the RF voltage about the synchronous particle. All of the particles are simultaneously accelerated due to the voltage being positive for all. This is the well-known phase stability and a principle of resonant acceleration in the RF synchrotron [5]. In this sense, the RF synchrotron may be called a combined-function accelerator in the longitudinal direction. This principle was independently recognized by McMillan [2] and Veksler [3] in 1945. However, a gradient focusing force is not the only possible way to achieve the longitudinal confinement of the particles. Electric fields, which are generated at both ends of the beam bunch using opposite sign voltages, as shown in Fig. 11.2, are capable of providing longitudinal focusing forces. A particle entering into a negative-voltage region, after drifting through a zero-voltage region, is decelerated and turns back to move toward the synchronous particle. It passes by the synchronous particle, while drifting with a constant energy along the time axis or the orbit axis. Once it reaches the positive voltage region, it is gradually accelerated, and again turns back towards the synchronous particle at the center of the bunch. The above process repeats every cycle of longitudinal synchrotron oscillation as the

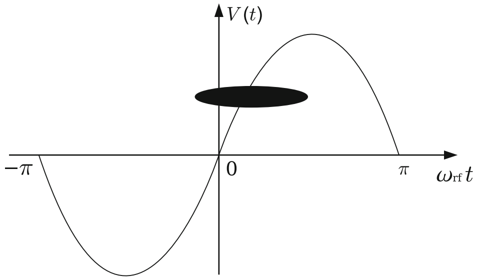

**Fig. 11.1** RF voltage and a bunch of charged particles

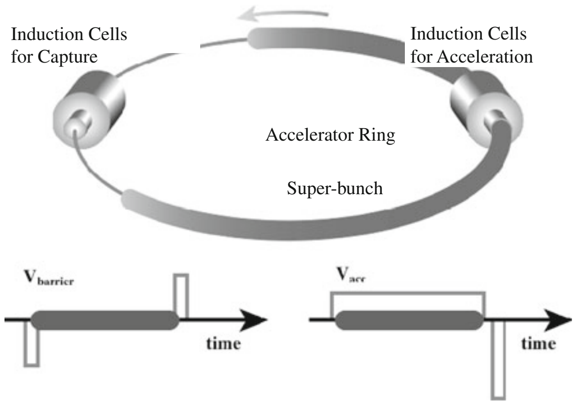

**Fig. 11.2** Schematic view of the Induction Synchrotron and step-voltage profiles for confining and acceleration

bunch goes through induction cells along the accelerator circumference. The process is nothing but phase stability. If an accelerating voltage pulse covering the time-duration between the pair of voltage pulses for longitudinal confinement is provided, the coherent acceleration of all the particles in the bunch will be guaranteed.

### 11.1.1 Review of Phase Dynamics in an RF Synchrotron

Here, we present a mathematical formulation to quantitatively understand the essential differences of longitudinal beam dynamics in the RF synchrotron and the Induction Synchrotron. The synchrotron oscillation for both cases is derived from discrete acceleration equations presented below. We assume that the RF and induction devices are localized at specific positions of the accelerator ring. The particle energy $E$ and phase $\phi$ are chosen as dynamical parameters to describe the particle motion. $E$ is the total energy of the particle of interest right before entrance into an acceleration gap and $\phi$ is the RF phase that the particle sees while passing through the gap. Then we have

$$\begin{aligned}(\Delta E)_{n+1} &= (\Delta E)_n + eV_{\mathrm{RF}}(\sin\phi_n - \sin\phi_n^s),\\ \phi_{n+1} &= \phi_n + \frac{2\pi h\eta}{(\beta^s)^2 E^s}(\Delta E)_{n+1} + (\phi_{n+1}^s - \phi_n^s) + \Delta\phi_{\mathrm{RF},n+1},\end{aligned} \tag{11.1}$$

with

$$(\Delta E) = E - E^s, \qquad \phi = \omega_{\mathrm{RF}} t, \qquad \eta = \frac{1}{\gamma_{\mathrm{T}}^2} - \frac{1}{\gamma_s^2},$$

Here, the subscript $n$ denotes the $n$-th turn and the superscript $s$ refers to quantities associated with the ideal synchronous particle, $h$ is the harmonic number, $\omega_{\mathrm{RF}}$ and $V_{\mathrm{RF}}$ are the angular frequency and voltage of the RF, $\eta$ is the so-called slippage factor, $\gamma_{\mathrm{T}}$ is the transition energy, and $\Delta\phi_{\mathrm{RF},n+1}$ is the shift of the RF phase which usually occurs at transition crossing. The set of the discrete equations are averaged over a time period for a single turn, $T_0 = 2\pi/\omega_0$, where $\omega_0$ is the angular rotation frequency of the synchronous particle. Introducing a convenient variable, $W = \Delta E/\omega_{\mathrm{RF}}$, we obtain a continuous equation of motion:

$$\begin{aligned} \frac{\mathrm{d}W}{\mathrm{d}t} &= \frac{eV_{\mathrm{RF}}}{2\pi h}(\sin\phi - \sin\phi^s), \\ \frac{\mathrm{d}\phi}{\mathrm{d}t} &= \frac{\omega_{\mathrm{RF}}^2\eta}{(\beta^s)^2E^s}W. \end{aligned} \tag{11.2}$$

For small-amplitude oscillations, we can define the well-known synchrotron frequency as follows. The upper equation is expanded in terms of $\Delta\phi \equiv \phi - \phi^s$. Since $\sin\phi - \sin\phi^s = \sin(\Delta\phi + \phi^s) - \sin\phi^s \cong \Delta\phi\cos\phi^s + \sin\phi^s - \sin\phi^s$, Eq. (11.2) reduces to

$$\begin{aligned} \frac{\mathrm{d}W}{\mathrm{d}t} &\cong \frac{eV_{\mathrm{RF}}\cos\phi^s}{2\pi h}\Delta\phi, \\ \frac{\mathrm{d}\Delta\phi}{\mathrm{d}t} &\cong \frac{\omega_{\mathrm{RF}}^2\eta}{(\beta^s)^2E^s}W. \end{aligned} \tag{11.3}$$

Taking the time-derivative of the lower equation and instituting the upper equation, we have

$$\frac{d^2\Delta\phi}{\mathrm{d}t^2} = \frac{\omega_{\mathrm{RF}}^2\eta}{(\beta^s)^2E^s}\frac{\mathrm{d}W}{\mathrm{d}t} = \frac{eV_{\mathrm{RF}}\omega_{\mathrm{RF}}^2\eta\cos\phi^s}{2\pi h(\beta^s)^2E^s}\Delta\phi. \tag{11.4}$$

Here, temporal changes in other parameters except for $W$ and $\Delta\phi$ are ignored. Thus, the synchrotron frequency is given as

$$\omega_s = \frac{\omega_{\mathrm{RF}}}{\beta^s}\sqrt{\frac{eV_{\mathrm{RF}}\eta\cos\phi^s}{2\pi hE^s}}. \tag{11.5}$$

The set of canonical equations in Eq. (11.2) can be obtained from the Hamiltonian,

$$H(\phi, W; t) = \frac{\omega_{\mathrm{RF}}^2\eta}{2(\beta^s)^2E^s}W^2 + \frac{eV_{\mathrm{RF}}}{2\pi h}\left[\cos\phi - \cos\phi^s + (\phi - \phi^s)\sin\phi^s\right]. \tag{11.6}$$

For a time-period sufficiently short, where temporal changes in the physics parameters for the synchronous particle are ignored, the Hamiltonian can be regarded as a constant of motion. We can obtain contour lines from $H(\phi, W; t) = H(\phi_0, W_0; t_0) = \text{const}$. A particle with a contour inside the separatrix shown in Fig. 11.3, is stably confined while accelerated. The area of the separatrix in phase space, is obtained by integrating the difference between the upper half and lower half of the phase volume in $\Delta p/p(\phi)$, bounded by the separatrix. The volume decreases with increasing magnitude of the synchronous phase $\phi^s$, assuming the RF voltage $V_{\mathrm{RF}}$ remains constant. The phase-space area available for acceleration is much less

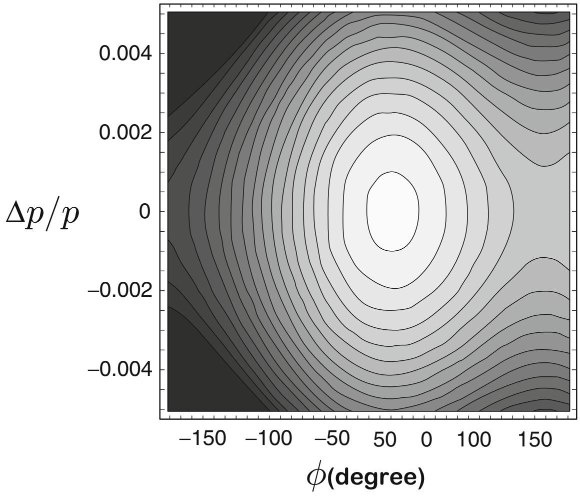

**Fig. 11.3** Hamiltonian contours in phase-space and the RF bucket

than $2\pi(\Delta p/p)_{\max}$, where $(\Delta p/p)_{\max}$ is the maximum height of the separatrix, suggesting that the total number of particles subject to acceleration is notably limited due to Liouville's Theorem. This is a fundamental limit of the RF synchrotron.

As mentioned, the temporal change in the synchronous phase is determined by $V_{\mathrm{RF}}$ and the ramped bending fields $B(t)$. The synchronous particle is subject to the force-balance in the transverse direction, $m\gamma^s c\beta^s = e\rho B$. where $\rho$ is the bending radius. $\gamma^s$ is uniquely determined by

$$\gamma^s = \sqrt{1 + \left[\frac{e\rho}{mc} B\right]^2}. \tag{11.7}$$

Consistent with this equation, the synchronous energy $E^s (= \gamma^s mc^2)$ changes according to the discrete equation:

$$E^s_{n+1} = E^s_n + eV_{\mathrm{RF}}(t) \sin\phi^s_n.$$

Averaging over the rotation period, we obtain

$$\begin{aligned} \frac{\mathrm{d}E^s}{\mathrm{d}t} &\cong \frac{E^s_{n+1} - E^s_n}{T_{n+1}} = \frac{eV_{\mathrm{RF}}(t)}{T_{n+1}} \sin\phi^s_n = \frac{eV_{\mathrm{RF}}(t)c\beta^s}{C_0} \sin\phi^s(t), \\ mc^2 \frac{\mathrm{d}\gamma^s}{\mathrm{d}t} &= \frac{eV_{\mathrm{RF}}(t)c\beta^s}{C_0} \sin\phi^s(t), \end{aligned}$$

where $C_0$ is the ring circumference and $T_{n+1} = C_0/c\beta^s_{n+1}$. This equation gives

$$\phi^s(t) = \sin^{-1}\left[\frac{mcC_0 \mathrm{d}\gamma^s/\mathrm{d}t}{eV_{\mathrm{RF}}(t)\beta^s}\right]. \tag{11.8}$$

From Eq. (11.7), we have

$$\phi^s(t) = \sin^{-1}\left[\frac{\rho C_0}{V_{\rm RF}(t)}\frac{{\rm d}B}{{\rm d}t}\right]. \tag{11.9}$$

The change in $\phi^s(t)$ is significant in a rapid cycling synchrotron. For a slow cycling synchrotron, it is almost constant over the entire acceleration time-period, except at the beginning and last stage of the acceleration.

### *11.1.2 Phase Dynamics in the Induction Synchrotron*

In an Induction Synchrotron, the required voltage pulses are generated by induction cells. Longitudinal bunch confinement and acceleration require different types of voltage-pulses, as shown in Fig. 11.2. The pair of the step-voltages shown in Fig. 11.2 has a focusing effect on the particles. A voltage with different polarity and the same height at the ends of the bunch is known as a barrier voltage. Barrier voltages were first proposed in the form of an isolated sinusoidal RF voltage by Griffin et al. [6], and experimentally realized by Blaskiewicz and Brennan [7]. In an Induction Synchrotron, the barrier voltage is introduced in the form of step-barrier voltages added to a circular ring. The step-voltage for acceleration has an asymmetric pulse profile, in which the pulse length has to be flexible to meet the various requirements of beam handling. The reset pulse may be short in time and high in voltage to keep the bunching factor large. It is noted that for both type of step voltages the integration of the voltage in time must always be zero in order to protect the magnetic core from saturating. The formulation for the step-barrier bucket acceleration is given below. The net voltage, which a particle entering into the devices with the phase $\phi = \omega_0 t$ experiences, is given by

$$V(\phi) = \begin{cases} V_{\rm ac} - V_{\rm bb} & (\phi^s - \Delta\phi/2) - \phi_{\rm pulse} \le \phi \le (\phi^s - \Delta\phi/2)\,, \\ V_{\rm ac} & (\phi^s - \Delta\phi/2) \le \phi \le (\phi^s + \Delta\phi/2)\,, \\ V_{\rm ac} + V_{\rm bb} & (\phi^s + \Delta\phi/2) \le \phi \le (\phi^s + \Delta\phi/2) + \phi_{\rm pulse}, \end{cases} \tag{11.10}$$

where $V_{\rm ac}$ is the accelerating voltage that is constant in time, $V_{\rm bb}$ is the barrier voltage, $\Delta\phi$ is the inner distance between the barrier voltages in phase, and $\phi_{\rm pulse}$ is the barrier pulse length. Then, the changes in energy and phase are given by discrete equations analogous to Eq. (11.1),

$$\begin{aligned} (\Delta E)_{n+1} &= (\Delta E)_n + e\,[V(\phi_n) - V_{\rm ac}]\,, \\ \phi_{n+1} &= \phi_n + \frac{2\pi\eta}{(\beta^s)^2 E^s}(\Delta E)_{n+1} + (\phi^s_{n+1} - \phi^s_n). \end{aligned} \tag{11.11}$$

In the continuous limit, Eq. (11.11) becomes

$$\begin{aligned}\frac{\mathrm{d}W}{\mathrm{d}t} &= \frac{e\left[V(\phi) - V_{\mathrm{ac}}\right]}{2\pi},\\ \frac{\mathrm{d}\phi}{\mathrm{d}t} &= \frac{\omega_0^2\eta}{(\beta^s)^2E^s}W.\end{aligned} \tag{11.12}$$

Here a convenient variable, $W = \Delta E/\omega_0$ is introduced. These canonical equations can be derived from the Hamiltonian,

$$H(\phi, W; t) = \frac{\omega_0^2\eta}{2(\beta^s)^2E^s}W^2 - \frac{e}{2\pi}\int^{\phi}\left[V(\phi') - V_{\mathrm{ac}}\right]\mathrm{d}\phi'. \tag{11.13}$$

The contours, which are orbits of the particles in phase space for fixed initial conditions, are shown in Fig. 11.4. The separatrix, which is called a barrier bucket, is clear. The contours inside the separatrix have a race-track, or almost rectangular, shape. Their figures in both sides are functions of the barrier parameters, such as $V_{\mathrm{bb}}$ and $\phi_{\mathrm{pulse}}$. Since $\Delta\phi$, by which the bunch-length is mainly determined, is a free parameter, one can control its length as desired insofar as it does not exceed the ring circumference and allows for reset time. This is a completely different feature from that of the RF-type synchrotron. This characteristic allows us, in principle, to have an almost circumference-long bunch in the accelerator ring, in principle. Such a long bunch has been called a *super-bunch*.

The synchrotron oscillation frequency for the Induction Synchrotron is defined in a similar manner to that in the RF synchrotron. However, the synchrotron frequency for a small amplitude does not make sense, because it fully depends on the longitudinal emittance as evaluated below. The synchrotron period consists of two parts.

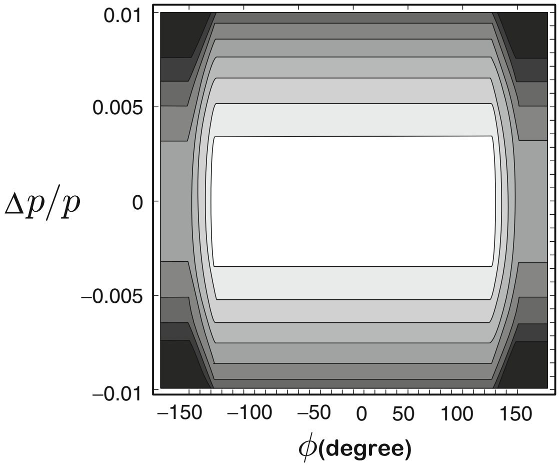

**Fig. 11.4** Hamiltonian contours in phase space and the barrier bucket

One results from the drift through the no-focusing region, and the other is from an oscillation period in a V-shape potential. Each of them is derived as follows. From Eq. (11.12), we straightforwardly have the drift time-period $\tau_d$,

$$\tau_d = \frac{2\Delta\phi(\beta^s)^2 E^s}{\omega_0^2|\eta|W} = \frac{2\Delta t}{|\eta|(\Delta p/p)}, \tag{11.14}$$

where $\Delta t = \Delta\phi/\omega_0$ is the time between the barrier pulses. The time-period $\tau_b$, within which a round trip in the V-shape potential takes, is obtained as follows. In this potential, the equations of motion are given by

$$\frac{\mathrm{d}W}{\mathrm{d}t} = -\frac{eV_{\mathrm{bb}}}{2\pi},$$
$$\frac{\mathrm{d}\phi}{\mathrm{d}t} = \frac{\omega_0^2\eta}{(\beta^s)^2E^s}W.$$

The second-order differential equation for $\phi$ and its solution with an initial condition of $\phi(0) = 0$ are

$$\begin{aligned}\frac{\mathrm{d}^2\phi}{\mathrm{d}t^2} &= -\left(\frac{eV_{\mathrm{bb}}}{2\pi}\right)\left[\frac{\omega_0^2\eta}{(\beta^s)^2E^s}\right] \equiv \kappa, \\ \phi(t) &= \frac{1}{2}\kappa t^2 + \dot{\phi}(0)t = t\left(\frac{1}{2}\kappa t + \dot{\phi}(0)\right).\end{aligned} \tag{11.15}$$

From Eq. (11.15), $\tau_b$ is obtained in the form of

$$\tau_b = -\frac{4\dot{\phi}(0)}{\kappa} = \left(\frac{8\pi}{eV_{\mathrm{bb}}}\right) = 4T_0\left[\frac{(\beta^s)^2E^s}{eV_{\mathrm{bb}}}\right]\left(\frac{\Delta p}{p}\right). \tag{11.16}$$

Thus, the synchrotron period $\tau_{\mathrm{sync}}$ in an Induction Synchrotron is given by

$$\tau_{\mathrm{sync}} = \tau_d + \tau_b = \frac{2\Delta t}{|\eta|(\Delta p/p)} + 4T_0(\beta^s)^2\left(\frac{E^s}{eV_{\mathrm{bb}}}\right)\left(\frac{\Delta p}{p}\right). \tag{11.17}$$

In the extreme relativistic limit with $\beta^s \cong 1$,

$$\tau_{\mathrm{sync}} \cong 2T_0\left[\left(\frac{\Delta t}{T_0}\right)\frac{1}{|\eta|(\Delta p/p)} + 2\left(\frac{E^s}{eV_{\mathrm{bb}}}\right)\left(\frac{\Delta p}{p}\right)\right]. \tag{11.18}$$

In most cases, the first term derived from the drift contribution dominates the synchrotron period. The synchrotron frequency is given by $f_s = 1/\tau_{\mathrm{sync}}$. The synchrotron frequency of a low-momentum particle is extremely small. It is shown later that this characteristic brings about a notable feature in phase mixing between particles, which takes a crucial role in coherent instabilities of a super-bunch.

The barrier-bucket height is one of the useful parameters when one considers barrier-bucket acceleration. Its height is obtained from the Hamiltonian as follows. The bucket height $W_{\max}$ satisfies

$$H(\phi_{\max}, 0; 0) \equiv 0 = \frac{\omega_0^2 \eta}{2(\beta^s)^2 E^s} W_{\max}^2 + \Phi(0), \tag{11.19}$$

where

$$\Phi(0) = -\frac{e}{2\pi} V_{\mathrm{bb}} \phi_{\mathrm{pulse}} = -\frac{e V_{\mathrm{bb}} \omega_0 \tau_{\mathrm{pulse}}}{2\pi}.$$

Here, $\tau_{\mathrm{pulse}}$ is the barrier pulse width. From Eq. (11.19), we have

$$\begin{aligned} W_{\max} &= \sqrt{\frac{(\beta^s)^2 E^s}{\omega_0 |\eta|} \frac{e V_{\mathrm{bb}} \tau_{\mathrm{pulse}}}{\pi}}, \\ \left(\frac{\Delta p}{p}\right)_{\max} &\equiv \frac{\omega_0 W_{\max}}{(\beta^s)^2 E^s} = \frac{\omega_0}{(\beta^s)^2 E^s} \sqrt{\frac{(\beta^s)^2 E^s}{\omega_0 |\eta|} \frac{e V_{\mathrm{bb}} \tau_{\mathrm{pulse}}}{\pi}} \\ &= \frac{1}{\beta^s} \sqrt{\frac{1}{|\eta|} \left(\frac{e V_{\mathrm{bb}}}{E^s}\right) \frac{2\tau_{\mathrm{pulse}}}{T_0}}. \end{aligned} \tag{11.20}$$

The expression in Eq. (11.20) suggests that the barrier bucket height is proportional to the square root of the product of the barrier voltage and its pulse length. It is useful to calculate the necessary value of $V_{\mathrm{bb}} \tau_{\mathrm{pulse}}$ for a given beam and ring parameters specified in terms of $(\Delta p/p)_{\max}$, $\eta$, $E^s$, and $T_0$.

## 11.2 Beam Handling

How is a super-bunch generated and accelerated in an Induction Synchrotron? What notable features of beam handling in the Induction Synchrotron are distinguished from that in the RF synchrotron? So far, a novel injection method, which makes the best use of step-barrier confining, has been proposed, and the feasibilities have been numerically investigated [1]. Here, the results of these studies are summarized. We consider a hadron accelerator complex, schematically shown in Fig. 11.5, consisting of an ion source, a pre-injector, such as RFQ, an $\mathrm{H}^-$ injector linac, a booster synchrotron, a second synchrotron, a third synchrotron, and a collider. Usually, the booster synchrotron is a rapid cycling synchrotron, and the following downstream synchrotrons are slow cycling synchrotrons. For simplicity, all synchrotrons belonging to the complex are assumed to be induction synchrotrons. For the convenience of readers, it is pointed out that FNAL has extensively developed beam handling techniques by the barrier voltages, which are generated in the wide-band RF cavity by a solid-state RF amplifier [8, 9]. Meanwhile, the idea of ion bunch confinement

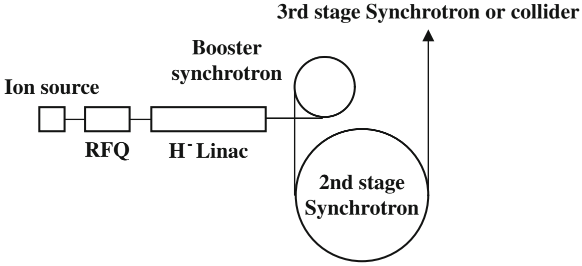

**Fig. 11.5** Schematic view of a hadron induction accelerator complex

utilizing ear-like fields, which is described in Sect. 9.2.4, have been proposed for the beam manipulation in a HIF beam driver. These beam handling techniques are similar to the barrier bucket beam manipulation given here, although there are big differences in their operational features or machine parameters.

### *11.2.1 Beam Injection*

For a rapid cycling synchrotron, a symmetric painting scheme is the most promising injection method in order to increase the injected beam intensity. This method takes a maximum advantage of the capacity of the barrier bucket. At first we consider chopped-mode $H^-$ injection. A macro-pulse is chopped from a continuous beam by a chopper located upstream of the injector $H^-$ linac, so that its pulse-length meets the barrier-pulse duration in the first synchrotron (booster) of the accelerator complex. The bunching mechanism in the $H^-$ linac converts the macro-pulse into a train of micro-pulses. Since a single-bunch mode of operation of the booster synchrotron is assumed, a single step-barrier bucket must be prepared for particle capture. Just after leaving the linac with the designed injection energy in the booster ring $E_{\text{inj}}$, the micro-pulse train enters into an RF cavity, which is called an energy splitter and operated at half of the linac RF-frequency. Consequently, the micro-pulse train is injected into the booster ring with a symmetric energy spread about $E_{\text{inj}}$, as shown in Fig. 11.6. Namely, the micro-bunches split into two groups in energy space. One group is the upper side in the barrier bucket, and the other is the lower side. By making the RF voltage of the energy splitter ramp in time or phase sweep, the barrier bucket is painted with micro-pulses through the injection process. Figure 11.7 shows a typical painting process in the longitudinal phase-space. In this example, the 3 GeV booster of the J-PARC facility in Japan [10] is chosen. The bunch trains injected earlier diffuse into a racetrack-shape ring, with a relative location in the phase-space determined by the injection timing. In this manner, a uniformly distributed long bunch, called a super-bunch, is created at the end of the injection process. The line density of the resulting super-bunch is shown in Fig. 11.7.

The bunching factor is one of the most important beam parameters when one considers the space-charge limit on the beam intensity. The bunching factor $B_f$

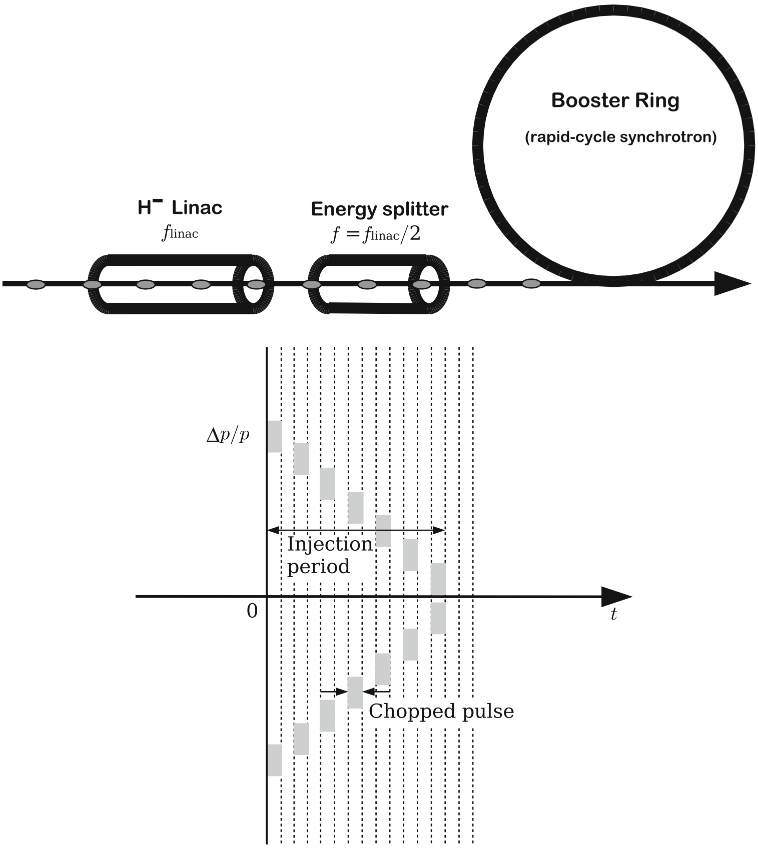

**Fig. 11.6** Symmetric painting

is defined by the ratio of average to peak beam intensity. Computer simulations indicate that a bunching factor of $B_f = 0.78$ is achievable at the end of the injection process. In an RF synchrotron driven with single harmonic RF, $B_f$ is typically between 0.25 and 0.3. For the case driven with dual harmonic RFs [11], $B_f$ is typically estimated to be around 0.4–0.5. As is well-known, the transverse space-charge beam limit for a particular synchrotron is quantified using the Laslett tune-shift, which is expressed in the following form when effects from the metallic aperture are neglected [12]:

$$\Delta\nu \propto \frac{Nh}{\beta\gamma^2 B_f \varepsilon}, \tag{11.21}$$

Here, $N$ is the number of particles per bunch, $h$ is the harmonic number ($h = 1$ for the Induction Synchrotron), and $\varepsilon$ is the normalized emittance. Usually, the magnitude of the space-charge tune-shift is limited to about 0.25. Note that the

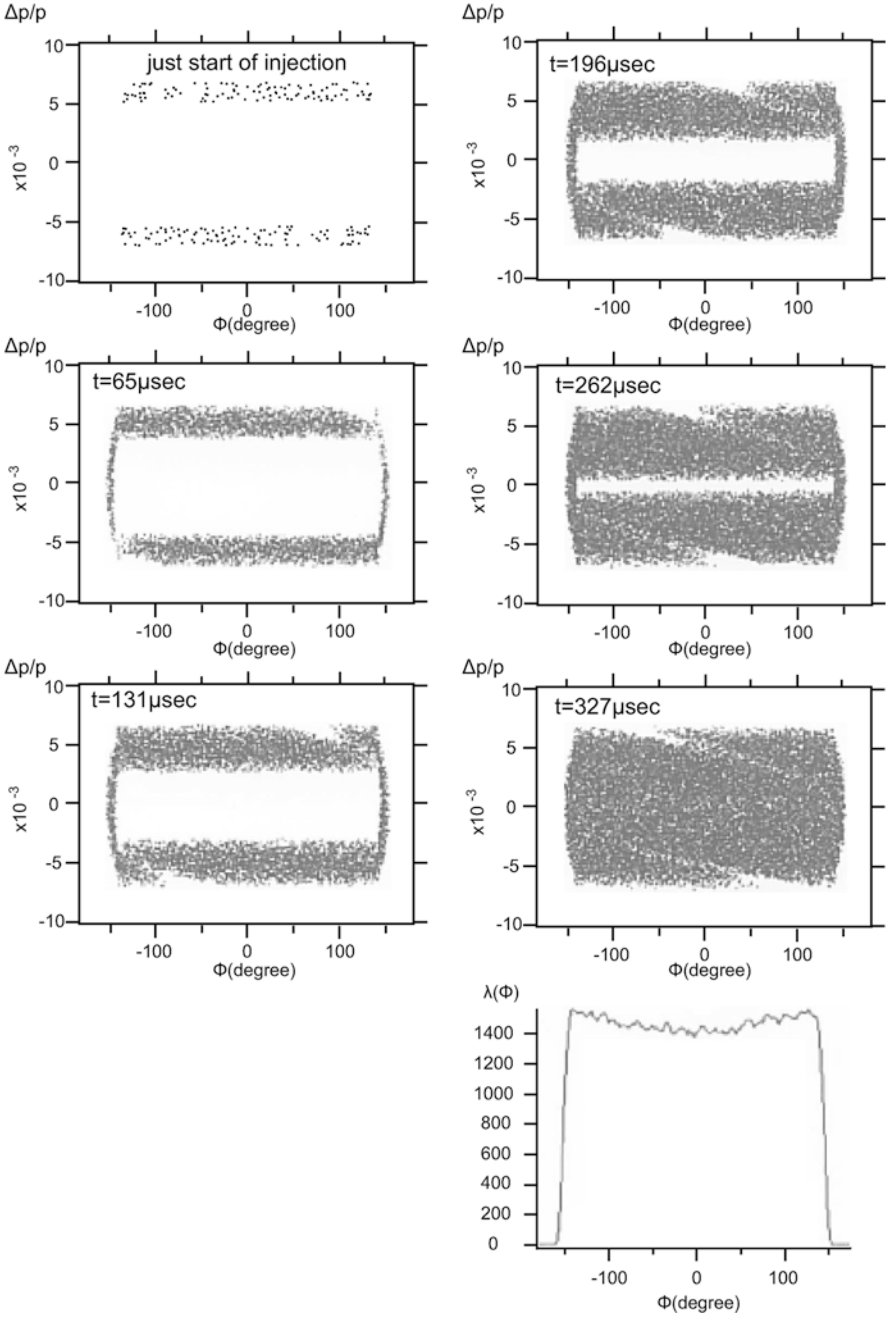

**Fig. 11.7** Computer simulation of symmetric painting in phase-space ($\phi$, $\Delta p/p$) for the J-PARC 3 GeV Ring. Phase space snapshots in time are shown from the first stage of injection to the last. The final line density of the super-bunch is also shown. Beam and machine parameters: $N = 8 \times 10^{13}$, $b/a = 1.8$ (averaged aspect ratio of the vacuum chamber), injection period of 330 $\mu s$, $h = 1$ (harmonic), $C_0 = 313.5$ m (circumference), $E_{\text{inj}} = 400$ MeV, $\gamma_{\text{T}} = 8.77$, $V_{bb} = 200$ kV (barrier voltage)

Laslett tune-shift is inversely proportional to $B_f$. Large $B_f$ allows a large value of $N$. In order to keep $\Delta\nu$ under the limiting value and increase $N$, increasing $B_f$ is a solution allowed by the super-bunch formed with the symmetric painting technique.

### 11.2.2 Beam Stacking and Super-Bunch Formation

Barrier bucket stacking of super-bunches in a slow cycling synchrotron is a natural progression. An upstream booster synchrotron delivers super-bunches at its operational cycle to a second downstream synchrotron. The transferred super-bunch is captured in a barrier bucket. Figure 11.8 shows a typical example of the stacking process. The captured super-bunch is adiabatically moved toward the stacking core. Then it is released at the location adjacent to the core by pausing trigger signals of the barrier pulse for capture. At the same time, the trigger signal of the reset pulse for the stacking barrier is delayed by the length of a subsequent injected super-bunch. Then, the subsequent super-bunch begins to merge into the core. The process is repeated until a single super-bunch with the desired length and momentum spread is formed for acceleration in this ring. This technique is applied in other downstream synchrotrons.

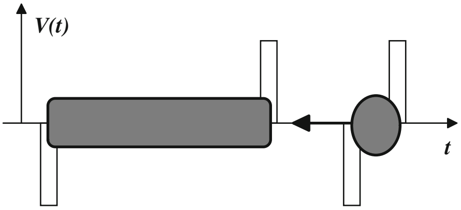

**Fig. 11.8** Schematic view of barrier-bucket stacking

### 11.2.3 Transition Crossing

At the transition energy, the polarity of the barrier-pulse is changed to provide longitudinal focusing without being interrupted in time. This is, in principle, same as a phase-jump in an RF synchrotron. This is achieved by changing the trigger timing of the barrier-pulses. Even in an Induction Synchrotron, problems arising from transition crossing, such as non-adiabatic phase motion, are analogous to those in an RF synchrotron. Both edges of the super-bunch extend in the momentum direction due to nonadiabaticity, as shown in Fig. 11.9, where the machine parameters of the KEK 12 GeV-PS are assumed. This phenomenon is caused by the fact that particles are being placed in the barrier regions continuously without the phase motion at transition. The barrier-bucket height can be controlled independently by reducing the barrier voltage in the vicinity of the transition energy without affecting the acceleration. Accordingly, one can avoid a deformed bunch shape with a large momentum spread, which may violate dispersive limits of the ring in some cases, as

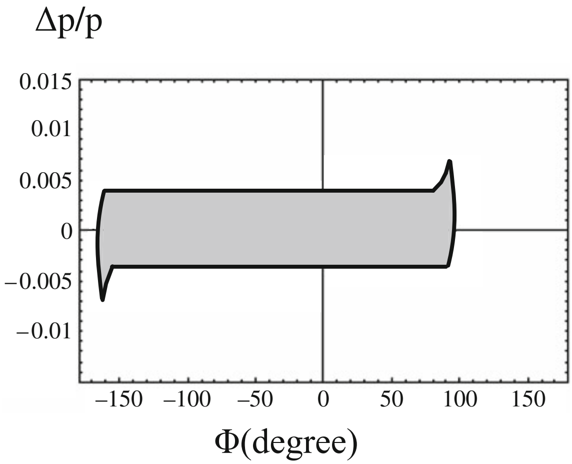

**Fig. 11.9** Super-bunch in phase space just at the transition energy. Both edges of the bunch are modified due to non-adiabaticity in the transition crossing process

shown in Fig. 11.9. Transition crossing in the Induction Synchrotron can be called *focusing-free transition crossing*.

It is instructive to compare focusing-free transition crossing in an Induction Synchrotron with nominal transition crossing in the RF synchrotron [13]. Nominal transition crossing in the RF case has caused various problems, such as an asymmetric bunch shape due to nonlinear kinematic effects [14–16], and microwave instabilities (see Fig. 11.10) in addition to non-adiabatic motion. The latter is caused when rapid increases of the beam line charge density, which is inevitable in the vicinity of the transition energy, are combined with narrow-band impedances distributed along the accelerator ring [17]. Results of a numerical simulation are shown in Fig. 11.10. Inclined bunch shapes caused due to the non-adiabaticity take place for every RF bucket. Here $h \neq 1$ is assumed. The line charge density increases by about 50% from that in a region far from the transition energy. Unfortunately, it is impossible to reduce the RF voltage in order to avoid these phenomena, because a constant acceleration rate has to be maintained. This is one of the disadvantages of a combined-function synchrotron in the longitudinal direction.

The Induction Synchrotron needs a long step-voltage pulse for acceleration, and a droop in such a long step-voltage pulse is typically inevitable. The droop is approximately modeled as a gradient in the voltage in time. The gradient causes longitudinal defocusing of a super-bunch below the transition energy, and longitudinal focusing above the transition energy. Simulation results assuming a few percent droop have indicated a fatal blowup in the longitudinal emittance of a super-bunch [18]. With respect to this point, super-bunch acceleration by a long step-voltage with droop is not conceivable. It is discussed in the literature [18] how such droop limitations can be counteracted. Super-bunch acceleration in an Induction Synchrotron may force us to reconsider a transition-free synchrotron lattice [10, 19], which requires many independently excited quadrupole magnets.

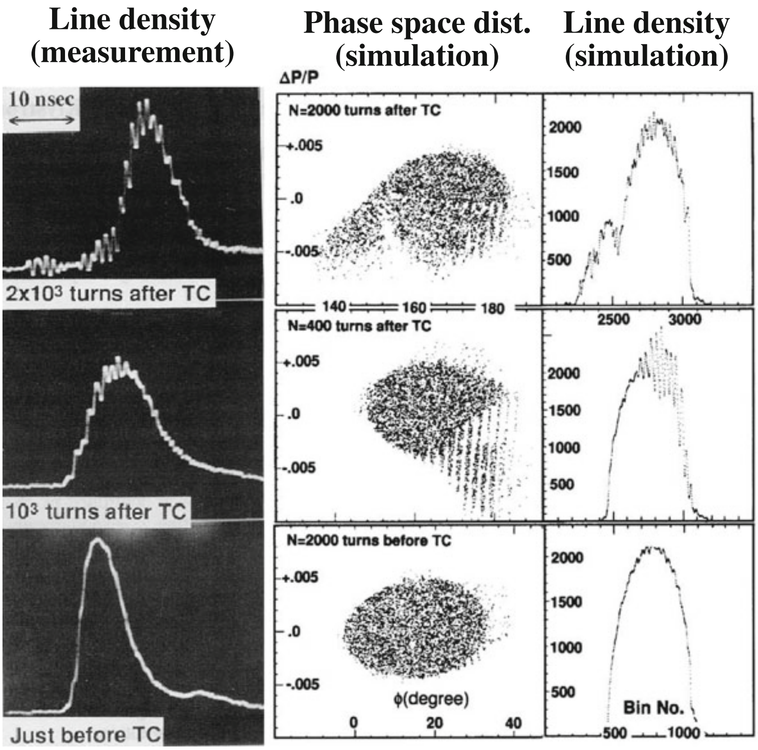

**Fig. 11.10** Typical microwave instability observed just above the transition energy [17]. TC means transition crossing

## 11.3 Induction Devices for an Induction Synchrotron

The key components required to realize an Induction Synchrotron are an induction accelerating cell and a pulse modulator driving the cell. These devices, however, are notably different from similar devices employed in linear induction accelerators that have been described in early chapters. The unique characteristics are the repetition rate and the duty factor. Another constraint is that the pulse modulator has to be positioned well outside the induction cell placed in the accelerator tunnel if high radiation is anticipated, because the solid-state power switching elements obtainable at present cannot survive high radiation dose. Thus, the pulse modulator which is later called the switching power supply needs to be connected with the accelerating cell through a long transmission cable to allow adequate shielding. In order to reduce reflections from the load, a matching resistance is installed at the end of the transmission cable. The induction accelerating system consists of an induction cell with a matching load, a transmission cable, a pulse modulator, and a DC power supply. A system capable of generating a step-pulse with 2 kV output voltage and 18 A output peak current at 1 MHz repetition frequency with 50% duty factor has been demonstrated at KEK [20].

### *11.3.1 Equivalent Circuit Model*

An equivalent-circuit model for the induction accelerating system is presented in Fig. 11.11, where all of the circuit components are connected in parallel. For simplicity, the circuit parameters are assumed to be independent of the frequency, and constant. The model for an induction cell and beam loading, which is in principle same as the equivalent circuit-model given in Chap. 3, will be described in Sect. 11.4.1.

The switching power supply is represented as a full-bridge switching circuit. $R$ is the resistance representing the core and eddy-current losses in the magnetic material. $L$ is the inductance, which is dominated by the magnetic material. $C$ is the cell capacitance, which is mainly determined by the mechanical cell structure including the ceramic gap, insulation materials, and coolant properties. The matching load $Z$ satisfies the first order matching condition,

$$\frac{1}{Z_0} = \frac{1}{Z} + \frac{1}{R},$$

where $Z_0$ is parallel to the cell and represents the characteristic impedance of the transmission cable. The energy stored in the primary capacitor bank is continuously charged by the upstream DC power supply and is transferred downstream in a programmed switching sequence synchronized with the circulation of the beam around the ring. Assuming that an idealized rectangular-shape pulse voltage is generated just after the switching power supply, the induced accelerating voltage between both terminals of the cell inductance is analytically obtained by solving a set of circuit equations modeling the transmission line shown below. Denote $V(t)$ and $I(t)$ as the voltage and current at the lower end of the transmission cable, and $I_Z$, $I_R$, $I_C$, $I_L$ as

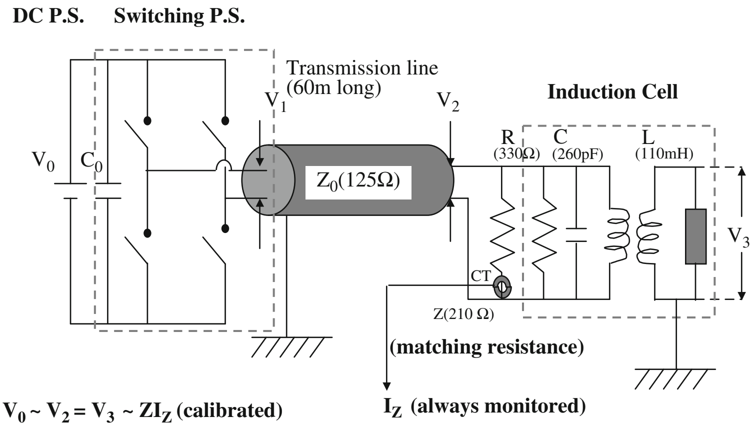

**Fig. 11.11** Equivalent circuit for the induction accelerating system

the current-flow through each labeled circuit component. Then circuit equations can be expressed as:

$$V(t) = Z \cdot I_Z = R \cdot I_R = \frac{1}{C}\int I_C \, \mathrm{d}t' = L\frac{\mathrm{d}I_L}{\mathrm{d}t}, \tag{11.22}$$

$$I(t) = I_Z + I_R + I_C + I_L. \tag{11.23}$$

Here, $V(t)$ and $I(t)$ are described by the terms of the forward/backward waves denoted with superscript +/- as follows: $V(t) = V^+(t) + V^-(t)$, $I(t) = I^+(t) + I^-(t)$, where $I^+(t) = V^+(t)/Z_0$ and $I^-(t) = -V^-(t)/Z_0$. Substituting these relations into Eqs. (11.22) and (11.23) and evaluating $I_Z, I_R, I_C$, and $I_L$ from Eq. (11.22), we obtain the following differential equation for $V^+(t)$ and $V^-(t)$:

$$\begin{aligned}\frac{1}{Z_0}(V^+ - V^-) &= \left(\frac{1}{Z} + \frac{1}{R}\right)(V^+ + V^-) + C(\dot{V}^+ + \dot{V}^-) \\ &\quad + \frac{1}{L}\int_0^t (V^+ + V^-)\mathrm{d}t'.\end{aligned} \tag{11.24}$$

Because the forward wave $V^+(t)$ is known, the backward wave $V^-(t)$ is uniquely determined by Eq. (11.24). The Laplace transform in time of $V^+(t)$ with initial conditions $V^+(0) = A$ and $\mathrm{d}V^+/\mathrm{d}t(0) = 0$ is $A/s$. The initial condition $V^+(0) = A$ gives $V^-(0) = -A$, because of $V(0) = 0$. If we denote the Laplace transform in time of $V^-(t)$ by $g(s)$ and a Laplace transform in time is made on Eq. (11.24), we obtain

$$\begin{aligned}\frac{1}{Z_0}\left(\frac{A}{s} - g\right) &= \left(\frac{1}{Z} + \frac{1}{R}\right)\left(\frac{A}{s} + g\right) + C(A + s \cdot g) \\ &\quad + \frac{1}{L}\left(\frac{1}{s}\frac{A}{s} + \frac{g}{s}\right).\end{aligned} \tag{11.25}$$

Here,

$$\int_0^\infty \frac{\mathrm{d}V^-(t)}{\mathrm{d}t} e^{-s \cdot t} \, \mathrm{d}t = -V^-(0) + s \cdot g(s) = A + s \cdot g(s)$$

is used. Evaluating $g(s)$ from Eq. (11.25), we have

$$g(s) = -A\frac{s^2 - (1/CZ_2)s + (1/CL)}{s \cdot \left[s^2 + (1/CZ_1)s + (1/CL)\right]}, \tag{11.26}$$

where $1/Z_1 = 1/Z_0 + 1/Z + 1/R$ and $1/Z_2 = 1/Z_0 - 1/Z - 1/R$. We calculate the inverse Laplace transform in time of $g(s)$ to obtain,

$$V^-(t) = -A\left[1 - \frac{2}{CZ_0\varphi}e^{-\gamma t}\sinh(\varphi t)\right], \tag{11.27}$$

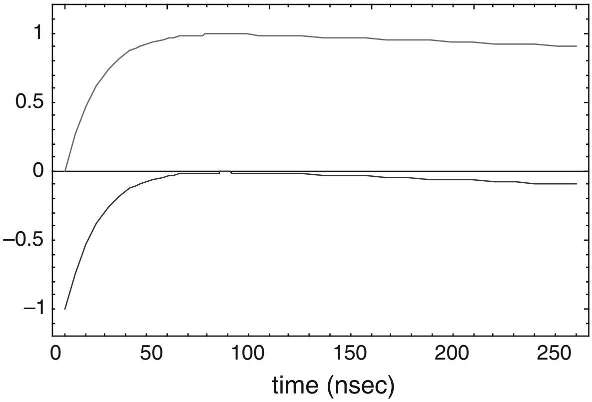

**Fig. 11.12** Normalized output voltage (*upper*) and reflected voltage (*bottom*)

where

$$\gamma \equiv \frac{1}{2Z_1C}, \qquad \varphi \equiv \frac{1}{2}\sqrt{\left(\frac{1}{Z_1C}\right)^2 - \frac{4}{LC}}.$$

Using Eq. (11.27) and assuming the circuit parameters of the KEK induction accelerating system described in Sect. 11.3.2, $V^-(t)$ and $V(t)$ are illustrated in Fig. 11.12.

The voltage rise time is determined by $C$ and the negative slope or droop in the voltage is approximated by $\exp(-Z_1t/L)$; it is a function of the magnitudes of $L$ and $Z_1$, where $Z_1$ is the equivalent impedance in Sect. 6.2. We can realize that the divergence of $V(t)$ from the incident rectangular pulse shape is caused by the backward wave. The backward wave propagates through the transmission cable, and is reflected at its other end with a different boundary condition, and returns to the side of the load. This process is repeated, while decreasing in magnitude due to power dissipation in the resistances. Details of the reflection ringing are omitted here. How the circuit elements are determined or chosen is now discussed.

### 11.3.2 Induction Cell

*Practical parameters*: The induction cells employed in the Induction Synchrotron are, in principle, the same as those used in a linear induction accelerator, which are described in detail in Chaps. 3 and 6. The induced voltage through the induction accelerating cell is described by Eq. (3.2) as

$$V\tau = -B_{\max}nS, \tag{11.28}$$

Here $S = wd$ is the cross-section of the single disk-shape magnetic material of thickness $d$ and width $w$, $V$ is the induced voltage across an induction accelerating cell consisting of $n$ disks (or bobbins if the magnetic material is thin tapes), $\tau$ is the pulse length, and $B_{\max}$ is the maximum flux. Assuming the required energy gain $\Delta E$ per turn, the number of induction accelerating cells required is determined by $n = \Delta E/(ZeV)$, where $Z$ is the charge state of ion. Since $\tau$ and $\Delta E$ are fixed by the machine requirement, the parameters of $n$, $B_{\max}$, and $S$ are optimized by minimizing the heat deposited in the magnetic material and the total cost consistent with any constraints on the available space in the beam-line.

*Magnetic material and cooling*: The choice of the magnetic material, as discussed in Chap. 5, is important. In a case of high repetition rate operation such as an Induction Synchrotron, a choice of low-loss material is essential. The core-loss depends on the magnetization rate $\mathrm{d}B/\mathrm{d}t$ and the actual flux swing $\Delta B$ ($\ll B_s$) different from the flux swing, $B_r + B_s$, shown in Sect. 5.4. Based on the magnetization models [21], a formula for the core-loss in a minor-loop excitation has been empirically obtained in the following form

$$\mathcal{E}\left[\frac{J}{m^3}\right] = (c_1 + c_2\Delta B)\left(\frac{d}{\rho}\right)\left(\frac{\mathrm{d}B}{\mathrm{d}t}\right)^{1/2} + c_3(\Delta B)^2\left[\frac{d^2}{(\rho B_s)}\right]\left(\frac{\mathrm{d}B}{\mathrm{d}t}\right). \qquad (11.29)$$

Here the first and second terms represent contributions from the bar-domain model and saturation wave model, respectively, $B_s$ is the saturation inductance in Tesla, $d$ is tape thickness in 10 μm, $\rho$ is resistivity of material in μΩm, and $\mathrm{d}B/\mathrm{d}t$ is in Tesla/μs. Coefficients of $c_1$, $c_2$, and $c_3$ depend on material. The parameters for a nanocrystalline material Finemet [22], which has been employed in the first experimental demonstration of the Induction Synchrotron, are:

Tape Thickness: $d = 1.6$ $c_1 = -0.44$
Resistivity: $\rho = 1.1$ $c_2 = 24.7$
Saturation Inductance: $B_s = 1.35$ $c_3 = 10.6$

Substituting the operating values of $\Delta B$ and $\mathrm{d}B/\mathrm{d}t$ into Eq. (11.29) and multiplying the result by a total volume of the magnetic core and a repetition rate, we can estimate the average power loss in Watts.

Cooling of the induction cell is a critical issue of the system design for high repetition rate. Cooling requirements depend on the type of magnetic material and which kind of coolant is acceptable. In the case of a nanocrystalline alloy such as Finemet, which is a conducting material and corrosive in water, the coolant can be air, electrically insulating inert perfluorocarbon fluid, insulating oil, or helium gas. It should be noted that the cell capacitance, which is a function of the dielectric constant of the coolant as well as the acceleration gap material, such as ceramic, determines the pulse rise and fall times, as shown in Eq. (11.27). In order to optimize the cooling efficiency, the temperature distribution in the induction cell is calculated by using a commercially available software package, such as ANSYS. Accordingly, the computer analysis aids the design of the cooling channel and coolant flow speed to maintain the magnetic core temperature below the critical point.

*Cell impedance*: In order to determine the actual cell impedance, specifically the cell inductance $L$, resistance $R$ representing the magnetization and eddy current losses, and capacitance $C$, three methods are normally used:

(1) Network-analyzer measurement assuming a LCR parallel circuit model and CW small amplitude excitation.
(2) Induced voltage measurement in a single pulse excitation.
(3) Measurements of voltage induced between the input terminals by a circulating beam.

First, we know the *inductance* and *resistance* in the AC mode excitation, $L(\omega) = [\mu' + (\mu'')^2/\mu']L_0$ and $R(\omega) = \omega[\mu'' + (\mu')^2/\mu'']L_0$, where the complex permeability, $\mu = \mu' - j\mu''$, of Finemet is known as a function of $\omega$ and provided by its manufacturer and $L_0$ is the core inductance in air taking account of the packing factor of the core material. The theoretical expression of the cell impedance in the parallel circuit model is given by $1/Z(\omega) = 1/R(\omega) + j[\omega C - 1/\omega L(\omega)]$ and the capacitance is independent of the drive frequency. We can determine the constant cell capacitance $C$ so as to fit the theoretical impedance curve as a function of $\omega$ to the result obtained by the method (1).

Since the induction cell is typically driven in the pulse mode with a large amplitude excitation, the most accurate values of $L$ and $R$ are obtained with pulse excitation with magnetization rates similar to those of the actual experiments.

2.5 *kV engineering model*: An induction cell [20] employed in the KEK 12 GeV synchrotron is shown in Fig. 11.13. The electrical parameters of each unit of the induction cell are given in the Sect. 11.4.1, which were determined from design considerations previously outlined [20]. Four unit-cells with a 2.5 kV output voltage per unit are mechanically combined into a single module for convenience of installation. Because the inner conductor with four ceramic gaps is common to four

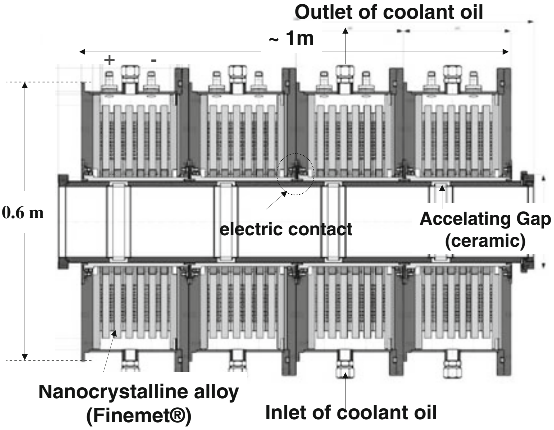

**Fig. 11.13** Quartet of induction cells (4 × 2.5 kV) employed in the KEK PS

unit-cells, but both sides of each gap are electrically connected to the outer edges of each cell, a particle is accelerated with the same voltage passing these gaps.

### 11.3.3 Switching Power Supply (Power Modulator)

*Full-bridge switching circuit*: For the barrier bucket, a full-bridge switching circuit, which is depicted in the equivalent circuit of Fig. 11.11, is employed because of its simplicity. The power modulator must be capable of generating bipolar rectangular shaped voltage pulses. A high repetition rate performance in the MHz range is required for typical applications. In addition, a fast rise/fall rate is required. Continuous wave (CW) high repetition rate operation is crucial for a ring. There are several solid-state switching elements capable of meeting these requirements as discussed in Chap. 4. A typical full-bridge type power modulator consists of four identical switching arms. Each switching arm is composed of several MOSFETs, arranged in series and parallel. The matrix of switching elements called a switching matrix hereafter, is determined by the allowed magnitudes of source-drain voltage and current capacity of each semiconductor switch. Their gates are driven by their own individual driving circuits, which are electrically isolated from their power source with extremely low capacitance DC–DC converters. The gate signals are generated by converting light signals provided from the pulse controller, which is a part of the accelerator control system, to electrical signals using TOS-Links (opto-electronic interface). To obtain a bipolar voltage, two sets of switching arms (S1/S3 and S2/S4) are turned on and off reciprocally.

Keeping intrinsic resonances of the modulator circuit away from the operating frequency is essential to obtain the desired flat-top voltage. For this purpose, the physical area encircled by the current flow is reduced to as small a value as possible so as to minimize the stray loop inductance in the circuit. The capacitance existing in the main circuit, which is dominated by the capacitance of MOSFETs, is responsible for a particular resonance. It is effective to reduce the number of columns in the switching matrix and increase line numbers in order to maintain a sufficient rise time. On the other hand, in order to reduce the diode current leading to heat loss in the MOSFETs, the driving current has to be divided into the columns of the switching Matrix. Optimized parameters of the switching matrix depend on the application of interest.

Heating of the MOSFETs and the gate driving ICs caused by CW MHz switching rates is large and must be addressed. Dissipation of 150 W per device are typical. Each pair of MOSFETs and gate driving ICs are mounted on a copper heat-sink. A DC voltage of 2.5 kV, supplied from the DC power supply, is distributed. Each MOSFET along a line shares a slightly different voltage due to the capacitances distributed in the entire circuit – including gate driving circuits. These elements include the equivalent capacitances between the source and drain, the FET and heat-sink, the heat-sink and ground, the FET and return circuit, and the gate circuit and ground. In particular, the capacitance of the DC–DC converter to isolate the gate circuit from the ground takes an important role in determining the voltage balance among the MOSFETs before closing the gates. Voltage imbalance is an important issue, because the loss at turn-on is proportional to the initial voltage balance. The maximum power loss (heat generated) occurs at the MOSFET having the maximum shared-voltage. When the heating exceeds some limit, such as the junction temperature of 150°C, the MOSFET will break down. The breakdown of a single MOSFET can cause the breakdown of other MOSFETs and failure of the switching arm, and the entire pulse modulator. An inclusive design guide-line and its experimental justification has been reported in [23, 24].

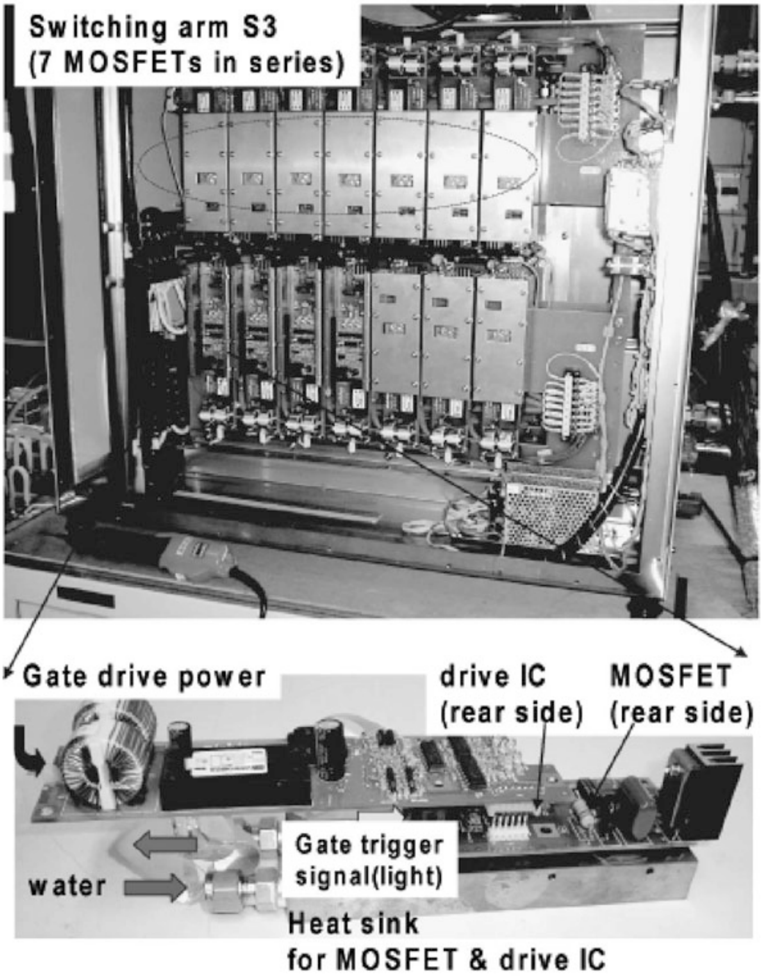

**Fig. 11.14** Photo of the KEK 2.5 kV switching power supply

As an example, the switching power supply, which was developed by KEK and Nichicon Kusatsu Co. Ltd., is shown in Fig. 11.14. Specifications of the switching power supply are:

| | |
|---|---|
| DC Power Supply: | 50 kW |
| Output Voltage: | 2.5 kV |
| Peak Output Current: | 21 A |
| Duty of Pulse: | 50% |
| Power Loss at MOSFET: | 200 W |

This switching power supply was successfully operated at a repetition rate of 1 MHz for 100 h, in which bipolar pulses of 2.0 kV output voltage and 250 ns pulse width were generated. The output voltage measured at the resistor load of 100 Ω is shown in Fig. 11.15. The 10–90% rise time and the 90–10% fall time were 20 and 25 ns, respectively. A flatness of 2% in the output voltage was obtained.

*Half-bridge switching circuit*: As mentioned earlier, a long set-pulse and short reset-pulse are required for super-bunch acceleration. A switching power supply capable of producing such a set of pulses employs a half-bridge switching circuit, in which two capacitor banks are required, as shown in Fig. 11.16. One provides a voltage for the accelerating pulse, and the other provides a higher voltage for the reset. The switching sequence is similar to that of the full-bridge switching circuit. A prototype has been demonstrated at Tokyo Institute of Technology [25, 21], in which the pulses have the same $V \times t$ product, so as to avoid core saturation. Output voltage measured is shown in Fig. 11.17. This switching architecture is conservative and the resistance of the system is determined by the higher reset voltage pulse.

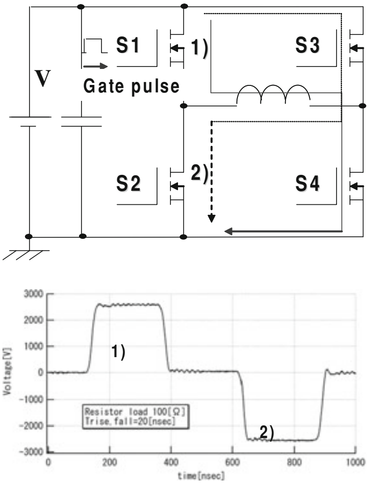

**Fig. 11.15** Output voltage of the KEK 2.5 kV switching power supply (see Fig. 11.14) with a resistive load of 100 Ω

**Fig. 11.16** Half bridge modulator

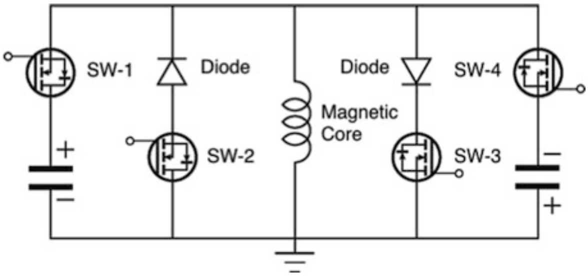

**Fig. 11.17** Experimental demonstration of asymmetric voltages

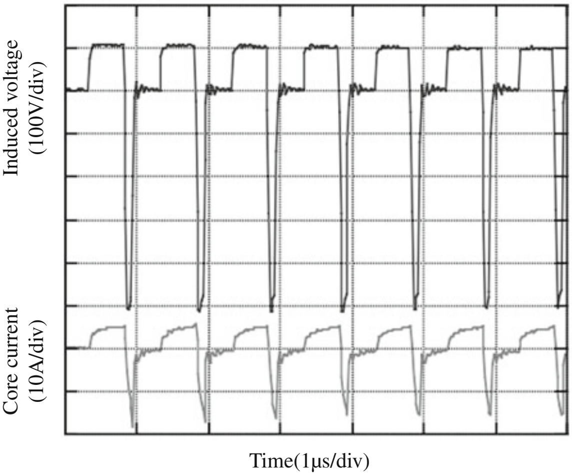

A simpler and more reliable circuit architecture has been developed at KEK. In this scheme, the acceleration voltage for a long-bunch is formed by summing the relatively short pulses in time. The short pulses are generated by bipolar switching power supplies and are summed by the induction cells by appropriate timing of the pulses as illustrated in Fig. 11.18.

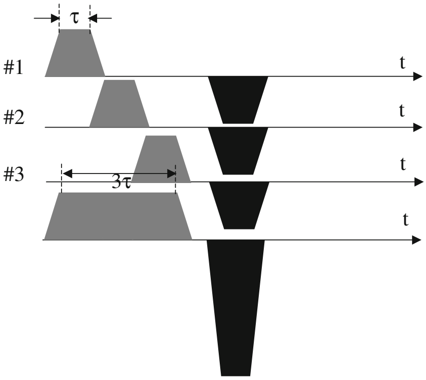

**Fig. 11.18** Superposition of the short-pulse induction voltages in time

## 11.4 Proof of Principle Experiment

Before the experimental demonstration of induction acceleration, the beam-cell interaction was investigated to establish the characteristics of the newly developed induction cell.

### *11.4.1 Beam–Cell Interaction: Beam Loading*

A high energy proton beam is an ideal driving source to confirm the electric parameters of the induction cell, because any steady-state interaction of the acceleration cell with the beam itself can be ignored in a single pass excitation. A simple experiment of the induction cell excitation by a single RF bunch was conducted using the KEK 12 GeV PS [26], where the induction cell described in Sect. 11.3.2 was installed without an external driver, and its feeder line was employed to monitor the induced voltage. The proton beam was captured in the RF bucket through the entire acceleration cycle. The bunch profile slowly changed during most of the acceleration cycle because of adiabatic damping. However, the bunch length rapidly shrunk when crossing the transition energy, as discussed in Sect. 11.2.3. Since the RF voltage was switched off after achieving flat-top energy, the bunch decayed into a DC beam due to the momentum spread in the bunch. The bunch shape and the induced voltage in time were observed at various times during the acceleration cycle. The former was monitored with an inductive fast current monitor and the latter was measured by a voltage probe connected between the terminals of the attenuating resistor. In this configuration, the induction cell is treated as a current transformer. Typical profiles of bunch shapes and the induced voltages measured are shown in Fig. 11.19. Similar data taken for other circuit parameters was employed to measure the circuit parameters of the induction cell.

The induced voltage $V(t)$ satisfies the following circuit equation for the equivalent circuit driven by a beam pulse:

$$\frac{\mathrm{d}^2V}{\mathrm{d}t^2} + \frac{1}{C}\left(\frac{1}{R} + \frac{1}{Z}\right)\frac{\mathrm{d}V}{\mathrm{d}t} + \frac{1}{LC}V = -\frac{1}{C}\frac{\mathrm{d}I_b}{\mathrm{d}t}, \tag{11.30}$$

Solved subject to the initial conditions $V(0) = 0$ and $\mathrm{d}V/\mathrm{d}t(0) = 0$. Here, $I_b$ is the beam current, $Z$ the external pure resistance to monitor the induced voltage, and $C^*$ the external capacitance connected in parallel to the cell and $C = C_0 + C^*$ with $C_0$, $R$, and $L$ are the intrinsic capacitance, resistance, and inductance of the cell, respectively. For simplicity, the frequency dependence of $R$ and $L$ is ignored. Making a precise estimate of $C_0$ and $R$ is not easy as mentioned in Sect. 11.3.2. However, $L \cong$ const is mostly determined from the geometrical parameters of the magnetic core and the core material properties. The solution of Eq. (11.30) is

$$V(t) = -\frac{1}{\beta C}\int_0^t \mathrm{d}t' e^{-\alpha(t-t')} \sinh\beta(t-t')\dot{I}_b(t'), \tag{11.31}$$

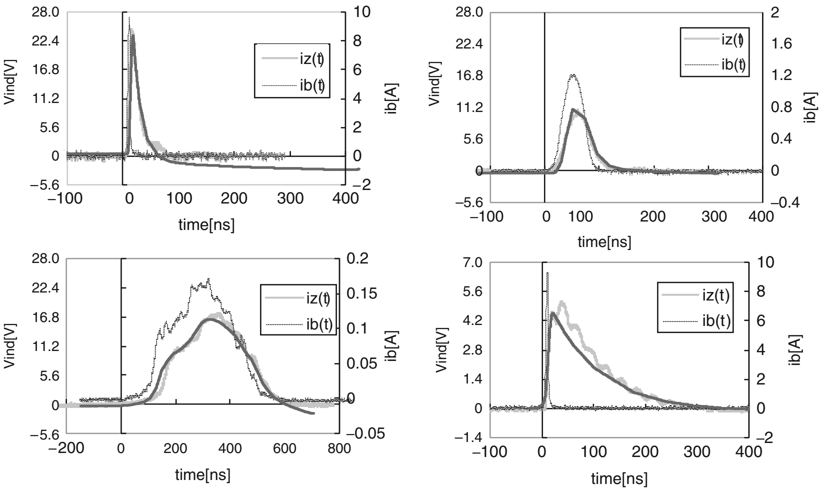

**Fig. 11.19** Induced voltage and beam-current profiles with corresponding approximate analytic solutions for $Z = 60\ \Omega$. The right bottom is for $Z = 60\ \Omega$ with an additional capacitance of $C = 1{,}000$ pF

where $\alpha$ and $\beta$ satisfy

$$\alpha = \frac{1}{2C}\left(\frac{1}{Z} + \frac{1}{R}\right), \qquad \alpha^2 - \beta^2 = \frac{1}{LC}.$$

Using the experimentally measured beam pulse profile into Eq. (11.31), we obtain an analytic expression for the induced voltage. The analytic calculations used the values

Capacitance: $C = 260$ pF
Resistance: $R = 330\ \Omega$
Inductance: $L = 110\ \mu$H

Comparisons of experimental and analytical results presented in Fig. 11.19 indicate good agreement, and consequently reasonable choices of circuit model parameters.

The induced voltage represents beam energy loss due to cell loading. The superbunch has an intensity gradient in both of its edges, as can be seen in Fig. 11.2, which constitutes a source of beam loading. The amount of beam loading can be easily estimated using Eq. (11.31) once the beam profile is given. If the peak beam current is many Amps, cell loading can be significant. Decreasing the cell impedance is effective to mitigate beam loading effects. Powerful switching power supplies capable of carrying higher driving currents are required, assuming the same output voltage.

### *11.4.2 Scenario of Proof of Principle Experiment*

Proof-in-principle experiments of the Induction Synchrotron concept were carried out using the KEK 12 GeV-PS [27] in 2004–2006. The experiment was divided into three stages:

(1) Induction acceleration of a single proton bunch captured in the RF bucket.
(2) Super-bunch formation in the barrier bucket.
(3) Induction acceleration of a single super-bunch captured in the barrier bucket.

These steps are sketched schematically in Fig. 11.20. In the first stage, a single bunch trapped in an RF bucket is accelerated with a total induction voltage of 10 kV up to the flat-top energy. Here, the RF is not responsible for the resonant acceleration, and its role is simply to capture particles. A trigger signal for the induction step-voltage pulse is controlled in a manner to synchronize the revolution frequency of the beam over the entire acceleration period. In the second stage, the role of the induction voltage is transferred to that of the barrier bucket, and a single bunch injected from the 500 MeV booster is captured in the barrier bucket, creating a 600 ns long bunch regarded as a pseudo super-bunch. Finally in the third step after further installation of induction modules, a full-demonstration of the induction synchrotron concept was carried out.

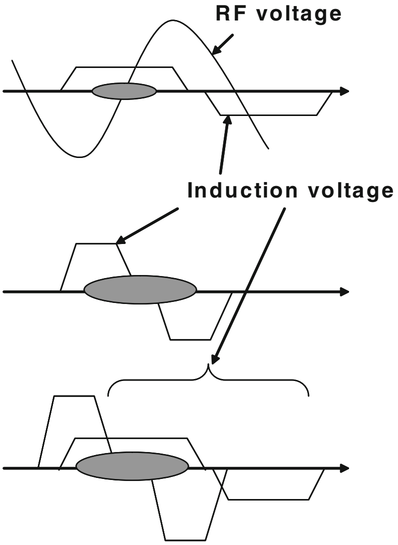

**Fig. 11.20** Staging in proof of principle experiments on the KEK 12 GeV PS. 1st step (*top*): RF trapping + induction acceleration (Hybrid synchrotron), 500 MeV → 8 GeV for $6 \times 10^{11}$ ppb, 2nd step (*middle*): Barrier trapping by induction step voltages at 500 MeV, 3rd step (*bottom*): Barrier trapping + induction acceleration (full induction synchrotron), 500 MeV → 6 GeV for $2 - 3 \times 10^{11}$ ppb

### *11.4.3 Induction Acceleration of an RF Bunch*

The system employed for the induction acceleration experiment is schematically shown in Fig. 11.21. The generation of a 2 kV voltage pulse is directly controlled by trigger pulses to the switching elements of the switching power supply. The master signal pulse is generated by the pulse sequencer of the digital signal processor (DSP) and is synchronized with the ramping of the bending magnets. Gate-driving signal patterns initiated by this master trigger signal are formulated through a pulse-pattern generator and sent to the gate controller of the switching power supply through a long coaxial cable. The pulse sequencer counts the so-called B-clock signal, which digitally counts the ramping of the guiding magnetic fields in time, and achieves the desired revolution frequency. Any delay between the accelerating pulse and a bunch monitor signal is compensated by the DSP in a programmed manner [28, 29]. The system is connected to the existing RF system through the RF signal, which shares the B-clock signal. As a consequence, a synchronized induction acceleration pulse is guaranteed. Here, the RF does not contribute to the acceleration of the beam bunch but gives the focusing force in the longitudinal direction; the beam bunch is longitudinally focused but not accelerated because the RF phase automatically adjusts to $\phi_s = 0$. The machine parameters of the KEK PS employed for the experiment are:

| | |
|---|---|
| Circumference: | $C_0 = 339$ m |
| Transition energy: | $\gamma_t = 6.63$ |
| Injection/extraction energy: | 500 MeV/8 GeV |
| Revolution frequency: | $f_0 = 668$–$877$ kHz |
| Ramping time (transient for start/stop): | 1.9 s (100 ms) |
| RF voltage: | $V_{\mathrm{RF}} = 48$ kV |
| Harmonic number: | $h = 9$ |
| Induction voltage per turn: | $V_{\mathrm{ind}} = 5.2$ kV |

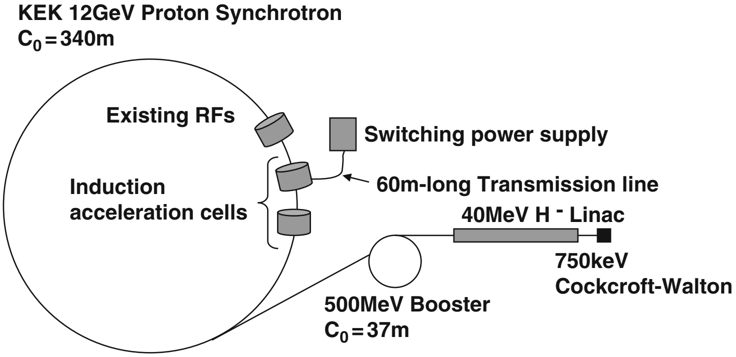

**Fig. 11.21** Schematic view of the hybrid accelerating system of the KEK PS

*Experimental results*: In the experiment [30], the bunch signals and signals from three current transformers (CT), which continuously monitor the current flow through the matching resistances, were displayed on the digital oscilloscope. Before the experiment, an induced voltage at a ceramic gap, an output voltage of the transmission cable, and the CT signals were simultaneously measured and the correspondence between each were well calibrated. In addition, a delayed timing of the master gate signal triggering the switching power supply was adjusted by the DSP so that the bunch signal would stay at the center of the induction voltage pulse throughout the entire acceleration cycle. Typical wave-forms of the CT signals are shown together with the bunch signal in Fig. 11.22.

*Theoretical background*: Under the influence of the RF voltage $V_{\mathrm{RF}}$ and the induction voltage $V_{\mathrm{ind}}$, a charged particle receives an energy gain per turn,

$$eV_{\mathrm{acc}}(t) = e\left[V_{\mathrm{RF}} \sin\phi(t) + V_{\mathrm{ind}}\right], \tag{11.32}$$

Here, $\phi(t) = \omega_{\mathrm{RF}} t$ is the position of the particle in the RF phase. The orbit and energy of a particle are described by the two equations. From the force balance in the radial direction we obtain

$$m\gamma \frac{(c\beta)^2}{\rho} = ec\beta B(t), \tag{11.33}$$

where $B(t)$ is the bending magnetic flux density and $\rho$ is the bending radius of the magnet. Second, from the change in energy of the reference particle

$$mc^2 \frac{\mathrm{d}\gamma}{\mathrm{d}t} = \frac{ec\beta}{C_0} V_{\mathrm{acc}}(t), \tag{11.34}$$

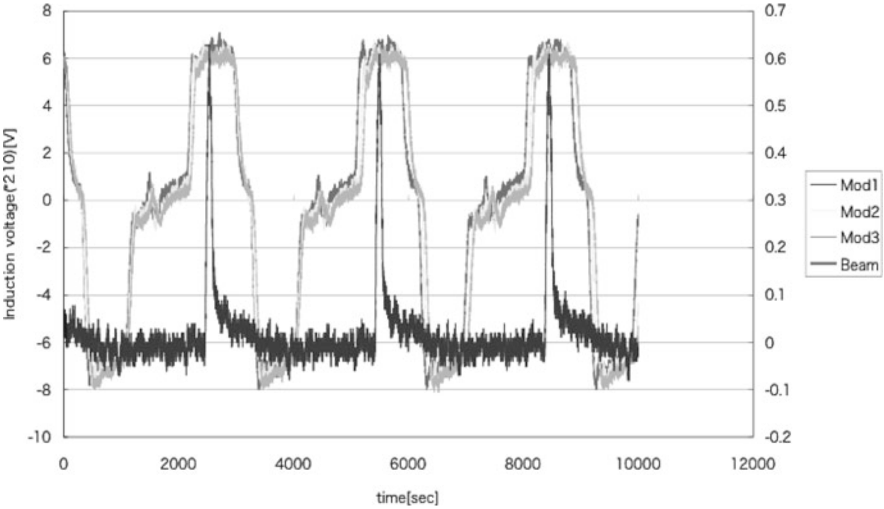

**Fig. 11.22** Induction pulse wave-forms (*gray*) and a bunch signal (*solid black*) from the KEK Proton Synchrotron experiment

where $C_0$ is the circumference of the ring. From Eqs. (11.33) and (11.34), the accelerating voltage must satisfy the relationship, $V_{\text{acc}}(t) = \rho C_0 \frac{\mathrm{d}B}{\mathrm{d}t}$, so that the particle is synchronously accelerated with ramped bending field. For the KEK proton synchrotron, the bending field is linearly ramped over 1.7 s and $V_{\text{acc}} = 4.7$ kV is required. For simplicity, the induction voltage was fixed to be close to 5.1 kV.

*Experimental observation*: In order to confirm the induction acceleration influence, the phase signal which shows the relative position of the bunch center to the RF was measured through the acceleration cycle. Particularly, we focused on three cases:

(1) RF voltage alone.
(2) RF voltage and a positive induction voltage.
(3) RF voltage and a negative induction voltage.

From Eq. (11.32), a theoretical prediction is $\phi_s = \sin^{-1}(V_{\text{acc}}/V_{\text{RF}}) \sim V_{\text{acc}}/V_{\text{RF}} = 5.7°$ for case (1), $\phi_s = -0.66°$ for case (2), and $\phi_s = \sin^{-1}(2V_{\text{acc}}/V_{\text{RF}}) \sim 2V_{\text{acc}}/V_{\text{RF}} = 12.4°$ for case (3). In case (2), since the induction voltage is devoted to the acceleration and the RF focuses the bunch without acceleration, $\phi_s$ must be zero. In case (3), the RF has to provide twice the energy to the bunch relative to case (1). It follows from energy-conservation that the phase should increase by a factor of two. Observed time-evolution of the phases through acceleration are presented in Fig. 11.23. Results indicate good qualitative agreement with the theoretical predictions. For both sides of the transition, the evolution in the phase difference is clearly understandable.

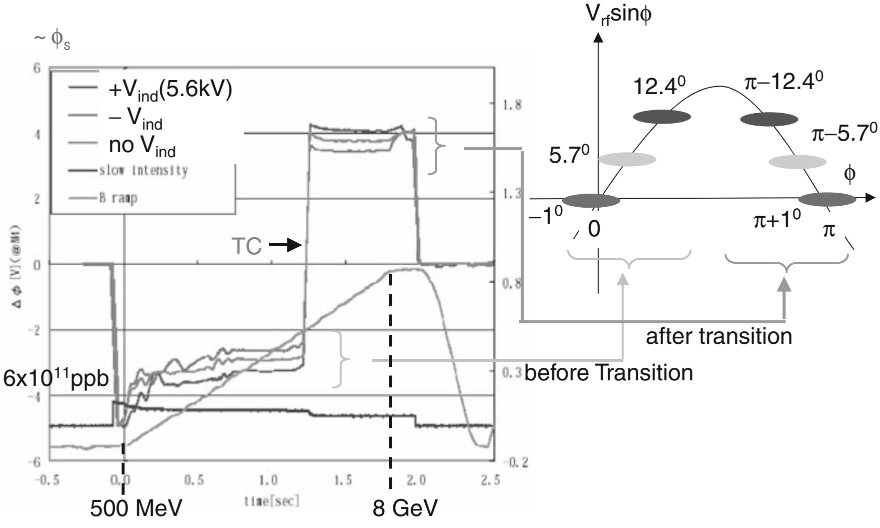

Fig. 11.23 Temporal evolution of the position of the bunch center in the RF phase

### *11.4.4 Confinement by Induction Barrier Voltages*

Beam confinement using induction step barriers, which is crucial to achieve a super-bunch, has been demonstrated using a shallow notch potential illustrated schematically in Fig. 11.24 [29]. A single proton bunch consisting of $5.0 \times 10^{11}$ protons was confined in the notch potential generated by the induction voltage $V_{\mathrm{barrier}} = 4.7$ kV, with a pulse width $T_{\mathrm{pulse}} = 400$ ns. Assuming a rectangular barrier voltage and $T_0 = 1.5$ μs, $\beta = 0.75$, $E_0 = (500 + 938)$ MeV at injection, Eq. (11.20) gives the bucket height in momentum space of $\Delta p/p = 0.27\%$. This height is slightly lower than the momentum spread of the injected proton bunch of 0.3%. Consequently, about half of injected protons were lost over 460 ms. Experimental results are shown in Fig. 11.25 for the temporal-evolution of the bunch shape from an injection energy of 500 MeV. The bunch remains trapped in the notch potential and stretches in time over 400 ms.

**Fig. 11.24** Schematic view of the notch potential and the trapped bunch profile

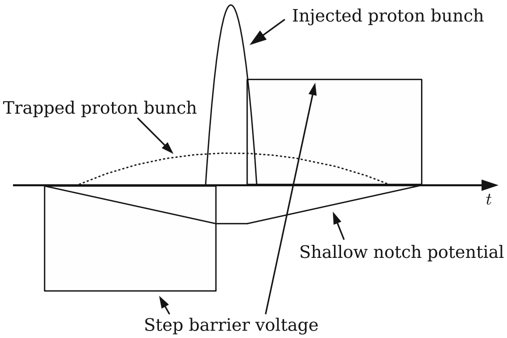

### *11.4.5 Induction Acceleration of a Trapped Barrier Bunch – Full Demonstration of the Induction Synchrotron*

The full-operation of an Induction Synchrotron requires a control system different from that of the hybrid synchrotron described in Sect. 11.4.3. Gate signals used to turn on the MOSFETs are generated by manipulating both signals monitored at the fast bunch monitor and the beam position monitors in a gate control system, which consists of a digital signal processor and active delay modules. This control system is illustrated in Fig. 11.26. Transverse beam-orbit control is the most important issue – as in any synchrotron. Without proper control, charged particles are not efficiently accelerated and can impact the vacuum chamber. The so-called ΔR-feedback system is equipped to meet this requirement in a conventional RF synchrotron, where the RF phase seen by the bunch center is automatically adjusted in real time to compensate any surplus or shortage of acceleration. A similar feedback control system is introduced for the Induction Synchrotron. In this system, the

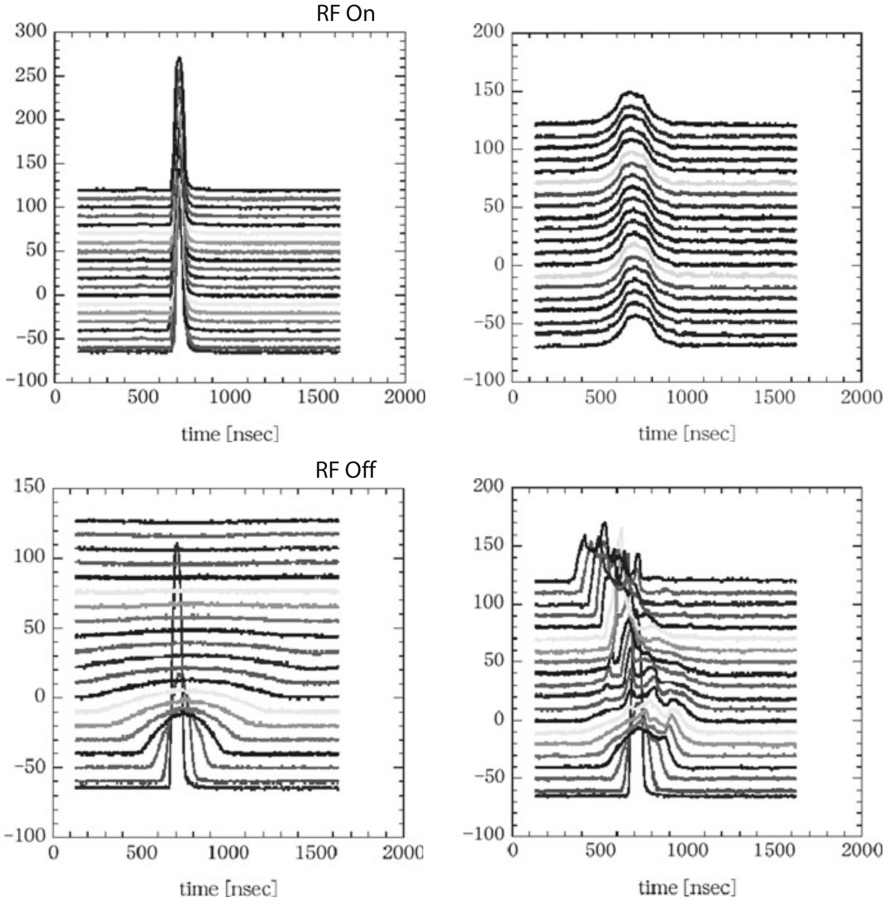

**Fig. 11.25** Mountain views of the injected pulse in time. *Lower left*: RF off and just debunching of the injected pulse every 50 turns. *Upper left*: RF on and just RF trapping at 150 ms after injection every 50 turns. *Lower right*: Barrier voltage on and barrier trapping of the injected pulse just after injection every 50 turns. *Upper right*: barrier trapping at 150 ms after injection every 50 turns

gate pulse generation is determined by integrating the digital gate pulse generator with the orbit information proportional to the momentum error, $\Delta p/p$. The position monitor directly gives $\Delta R = D(s)\Delta p/p$, where $D(s)$ is the momentum dispersion function at the location of the position monitor [12]. When the signal amplitude exceeds a preset threshold value, the gate trigger signal is blocked in the DSP. Accordingly, the acceleration voltage pulse is not generated on subsequent turns until the momentum approaches the correct value, which is uniquely determined by the bending field. Note that the induction acceleration voltage per turn is always set to be a bit larger than the required voltage $\rho C_0 \mathrm{d}B/\mathrm{d}t$. The integrated gate control system is depicted in Fig. 11.26.

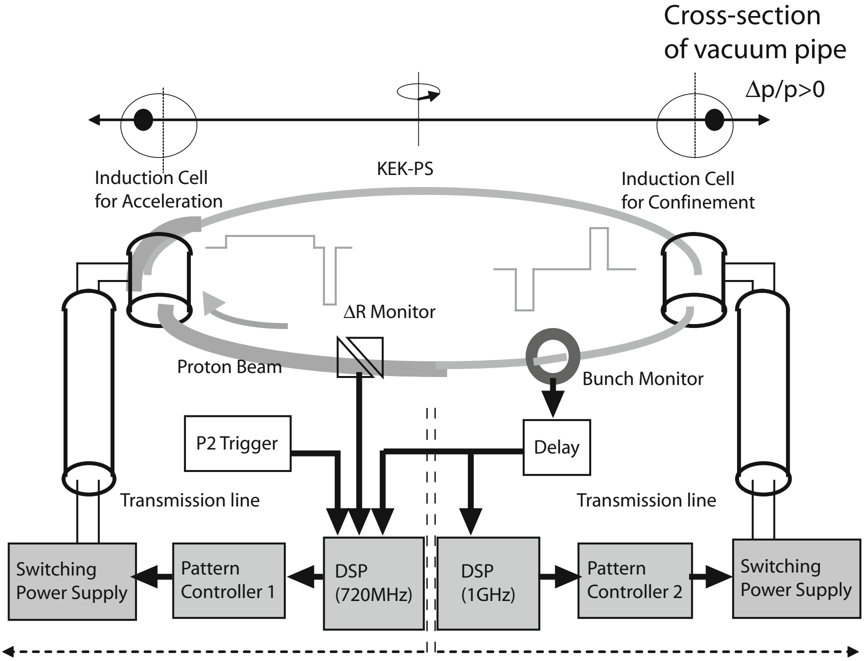

**Fig. 11.26** Gate control system. P2 is timing of acceleration start

A typical example of the acceleration in the Induction Synchrotron [31] is presented, where a single 100 ns-long bunch injected from the KEK 500 MeV Booster Ring into the KEK PS was trapped in the barrier voltages shown in Fig. 11.27. The half-momentum spread of the injected beam is $(\Delta p/p)_{\max} = 0.003$ determined by measuring a debunching time of the injected beam in the KEK PS. The barrier voltages create a barrier bucket with height

$$\left(\frac{\Delta p}{p}\right)_{\text{height}} = \sqrt{\frac{2eV_{\text{bb}}\tau}{\beta^2 ET|\eta|}}. \tag{11.35}$$

Here, $V_{\text{bb}}$ is the barrier voltage, $\tau$ the pulse width of the barrier voltage, $\eta$ the slippage factor and $\beta$, $E$, and $T$ are the relativistic beta, total energy, and revolution period of the synchronous particle, respectively. The net $V_{\text{bb}} = 1.8$ kV $\times 6 = 10.8$ kV was sufficient to accommodate the injected bunch. However, the injected bunch captured by the RF bucket in the Booster ring did not match the barrier-bucket shape. Due to transient filamentation-process in the longitudinal phase-space resulting in a bunch length of 400 ns, the bunch was trapped in the barrier bucket during 450 ms just after injection. The trapped bunch was then accelerated to 6 GeV, consistent with the ramping field $B(t)$ of the guiding magnets. Because the KEK PS is operated as a slow cycling synchrotron, the ramping pattern is divided into three

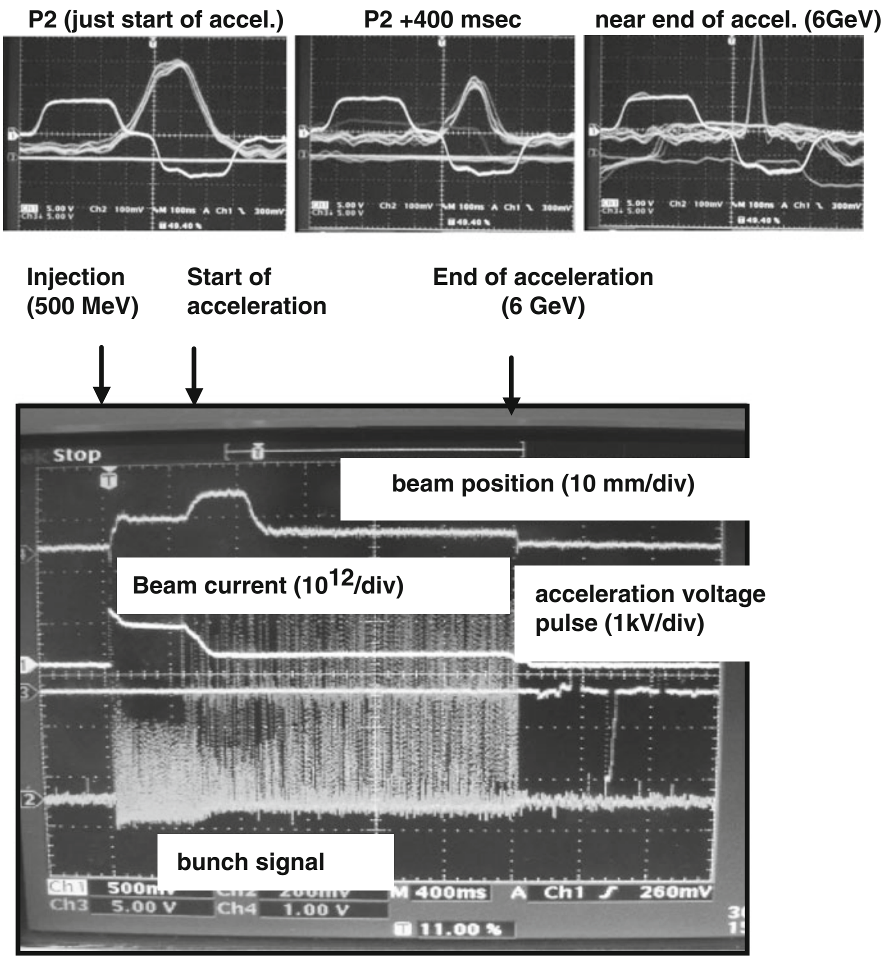

**Fig. 11.27** (a) From *left* to *right*: Proton bunch trapped by step barrier voltages before acceleration, in the middle of acceleration, and at the end of acceleration. Gaussian-like, bunch signal; step barrier voltage with opposite polarity; acceleration voltage pulse with a long pulse shape. (b) Ch1, beam current ($10^{12}$/div); Ch2, bunch monitor signal (the amplitude is inversely proportional to the bunching factor); Ch3, gate pulse density vs. time; Ch4, central beam position ($\Delta$R) (10 mm/div)

regions comprising two transient regions corresponding to the acceleration start and end and the long linear ramping region. The required accelerating voltage to follow this ramping pattern is described by $V_{\mathrm{acc}} = \rho C_0 \frac{\mathrm{d}B}{\mathrm{d}t}$, where $\rho$ is the bending radius, $C_0$ is the circumference of the accelerator, and $B$ is the bending magnetic flux density as a function of time. Four induction acceleration cells with an output voltage of 1.6 kV per cell were employed for acceleration. The total accelerating voltage of 6.4 kV provided by the induction acceleration cells was much larger than 3.12 kV required in the linear ramping region. A substantial beam loss at the early stage of acceleration is apparent in the second trace of Fig. 11.27b. Beyond that initial period, the beam intensity remained constant without any beam loss. From the previous experiment [29] described in Sect. 11.4.4, it is known that the mismatch between the bunch shape and the barrier bucket creates a fine-structure in the beam profile in time, yielding a signal from the bunch monitor with the same structure. This effect sometimes caused a timing error in the gate signal for the confinement barrier voltages, leading to a kind of bucket jitter. This occurs because the gate trigger signal is generated when the bunch signal exceeds the preset value in the gate control system and a local peak isolated from the bunch center happens to exceed this threshold. It is speculated that this mechanism is the cause of the beam loss just after injection. The other beam loss at the beginning of acceleration appears to be caused by insufficient $\Delta R$ feedback in the transient region approaching the linear ramping region. The outer edge of the beam in the horizontal direction may scrape the vacuum chamber. The bunch length gradually decreased with acceleration. Eventually it approached about 100 ns near the transition energy at 6 GeV. This is the expected adiabatic characteristics confirmed by a computer simulation assuming realistic barrier voltage parameters [32]. Throughout the entire acceleration, the central orbit of the bunch was kept at a constant value, as expected. The result is shown by the upper trace in Fig. 11.27b.

## 11.5 Perspective

As discussed in Chap. 12, various applications have been considered since the first proposal of the Induction Synchrotron. The super-bunch hadron collider or a proton driver for the second generation of neutrino oscillation experiments are among them. These applications rely on the realization of a super-bunch, the line density of which is just under the space-charge limit in the transverse direction. For this purpose, a long pulse-duration between the barrier voltages and a long pulse acceleration induction voltage is required. The induction acceleration module should be low impedance to minimize beam-loading effects due to a large increase in the stored beam current. The switching power supply used to drive such a low-impedance device must be capable of carrying larger arm currents. The arm currents are limited by the capability of the switching element employed. Research and development on a high-current switching power supply employing newly developed solid-state switching elements, such as a mold-type SI thyristor or a SiC-JFET, are being conducted in a collaboration with high-energy physics institutes, universities, solid-state material industries, and pulsed-power industries [33].

The Induction Synchrotron concept has been demonstrated in a complete manner, although there are still some unexplained phenomena. It can be concluded that the concept has been confirmed and this acceleration technology will promise a next generation of accelerator. Assuming further developments in the key devices, novel applications never realized in a conventional RF synchrotron will be expected in the future.

## References

1. K. Takayama and J. Kishiro. Induction Synchrotron. *Nucl. Inst. Meth. A*, A451:304–317, 2000.
2. E. McMillan. The Synchrotron. A Proposed High Energy Particle Accelerator. *Phys. Rev.*, 68:143, 1945.
3. V. Veksler. A New Method of Acceleration of Relativistic Particles. *J. Phys. USSR*, 9:153–158, 1945.
4. S. D. Putnam. Survey of Compact High Current Electron Accelerators. In *Proceedings of the 1987 Particle Accelerator Conference*, pages 887–891, Washington, DC, 16–19 March 1987.
5. H. Wiedemann. *Particle Accelerator Physics*. Springer, Berlin, 2007.
6. J. Griffin, C. Ankenbrandt, J. MacLachlan, and A. Moretti. Isolated Bucket RF Systems in the Fermilab Antiproton Facility. *IEEE Trans. Nucl. Sci.*, NS-30:3502, 21–23 Mar. 1983.
7. M. Blaskiewicz and J. Brennan. A Barrier Bucket Experiment for Accumulating De-bunched Beam in the AGS. In *Proceedings of the 1996 European Particle Accelerator Conference*, page 2373, Barcelona, Spain, 10–14 June 1996.
8. C.M. Bhat. Applications of Barrier Bucket RF Systems at FERMILAB. *Proceedings of the International Workshop on Recent Progress in Induction Accelerators*, pages 45–59, Tsukuba, Japan, 7–10 March 2006, KEK.
9. W. Chou and D. Wildman. Induction Barrier RF and Applications in Main Injector. *Proceedings of the International Workshop on Recent Progress in Induction Accelerators*. pages 106–111, Tsukuba, Japan, 7–10 March 2006, KEK.
10. F. Noda. 3 GeV RCS at the JKJ. In *AIP Conference Proceedings No. 642*, pages 53–55, Batavia, IL, 8–12 Apr. 2002. FNAL, American Institute of Physics.
11. C. Prior. Studies of Dual Harmonic Acceleration in ISIS. In *Proceedings of the 12th Meeting of the International Collaboration on Advanced Neutron Sources*, pages 4–11, Abington, UK, 24–28 May 1993. RAL.
12. D. Edwards and M. Syphers. *An Introduction to the Physics of High Energy Accelerators*. Wiley, New York, NY, 1993. For instance, see page: 176.
13. E. Courant and H. Snyder. Theory of the Altaernating Gradient Synchrotron. *Ann. Phys*, 3:1, 1958.
14. K. Johnsen. Effects of non-linearities on the phase-transition. In *Proceedings of the CERN Symposium on High-Energy Accelerators 1*, pages 106–111, Geneva, Switzerland, 11–23 June 1956. CERN.
15. K. Takayama. Phase Dynamics near Transition Energy in the Fermilab Main Ring. *Part. Accel.*, 14:201, 1984.
16. J. Wei. *Longitudinal Dynamics of the Non-Adiabatic Regime on Alternative-Gradient Synchrotrons*. PhD thesis, State University of New York at Stony Brook, 1990.
17. K. Takayama, D. Arakawa, J. Kishiro, K. Koba, and M. Yoshii. Microwave Instability at Transition Crossing: Experiments and a Proton-Klystron Model. *Phys. Rev. Lett.*, 78:871, 1997.
18. Y. Shimosaki, E. Nakamura, K. Takayama, K. Torikai, K. Horioka, M. Nakajima, and M. Watanabe. Beam-Dynamic Effects of a Droop in an Induction Accelerating Voltage. *Phys. Rev. Spec. Topics Accel. Beams*, 7:014201–014208, 2004.
19. B. Erdelyi and C. Johnstone. Tracking of Three Variants of Transition-Free Lattices for a Proton Driver. *In Proceedings of the 20th ICFA Advanced Beam Dynamics Workshop on High Intensity and High Brightness Hadron Beams ICFA-HB2002, AIP Conference Proceedings No. 642*, pages 146–149, Batavia, IL, 8–12 Apr. 2002. FNAL.
20. K. Torikai, Y. Arakida, E. Nakamura, T. Kono, Y. Shimosaki, T. Toyama, M. Wake, J. Kishiro, and K. Takayama. Induction Acceleration System for a Proton Bunch Acceleration in the KEK Proton Synchrotron. In *Proceedings of the 2005 Particle Accelerator Conference*, pages TPPT014, 1679–1681, Knoxville, TN, 16–20 May 2005.

21. M. Watanabe, K. Horioka, J. Kishiro, M. Nakajima, M. Shiho, and K. Takayama. Magnetic Core Characteristics for High Rep-Rate Induction Modulator. *Rev. Sci. Inst.*, 73:1756–1760, 2002.
22. S. Nakajima, S. Arakawa, Y. Yamashita, and M. Shiho. Fe-Based Nanocrystalline FINEMET Cores for Induction Accelerators. *Nucl. Inst. Meth. A*, 331:5556, 1993.
23. K. Koseki, K. Takayama, and M. Wake. Significance of Isolation Impedance in a Solid-state Power Modulator. *Nucl. Inst. Meth. A*, 554:64, 2005.
24. M. Wake, Y. Arakida, K. Koseki, Y. Shimosaki, K. Takayama, K. Torikai, W. Jiang, K. Nakahiro, A. Tokuchi, and A. Sugiyama. Swithing Power Supply for Induction Accelerators. In *Proceedings of the 2007 Particle Accelerator Conference*, pages MOPAN042, 251–253, Albuquerque, NM, 25–29 June 2007.
25. M. Watanabe. *Induction Voltage Modulator with Cotrollability and Repetition Capability*. PhD thesis, Tokyo Institute of Technology, 2002.
26. K. Torikai, K. Koseki, E. Nakamura, Y. Shimosaki, Y. Arakida, T. Kono, T. Toyama, M. Wake, and K. Takayama. Induction Accelerating Cavity for a Circular Ring Accelerator. In *Proceedings of the 2004 European Particle Acclerator Conference*, pages MOPLT066, 704–706, Lucerne, Switzerland, 5–9 July 2004.
27. K. Takayama, J. Kishiro, K. Koseki, K. Torikai, E. Nakamura, T. Toyama, Y. Arakida, M. Wake, H. Sato, M. Shirakata, S. Igarashi, Y. Shimosaki, M. Sakuda, D. Iwashita, K. Horioka, and M. Shiho. A POP Experiment Scenario of Induction Synchrotron at the KEK 12 GeV-PS. In *Proceedings of the 2003 Particle Accelerator Conference*, pages TPPB093, 1807, Portland, OR, 12–16 May 2003.
28. K. Torikai, K. Takayama, Y. Shimosaki, J. Kishiro, and Y. Arakida, Patent 2005198557 in Japan.
29. K. Torikai, K. Takayama, Y. Shimosaki, Y. Arakida, E. Nakamura, D. Arakawa, S. Igarashi, T. Iwashita, A. Kawasaki, J. Kishiro, K. Koseki, T. Kono, H. Sato, M. Shirakata, T. Sueno, A. Tokuchi, T. Toyama, and M. Wake. Acceleration and Confinement of a Proton Bunch with the Induction Acceleration System in the KEK Proton Synchrotron. Technical Report KEK Preprint 2005-80, KEK, 2005.
30. K. Takayama, K. Koseki, K. Torikai, A. Tokuchi, E. Nakamura, Y. Arakida, Y. Shimosaki, M. Wake, T. Kouno, K. Horioka, S. Igarashi, T. Iwashita, A. Kawasaki, J. Kishiro, M. Sakuda, H. Sato, M. Shiho, M. Shirakata, T. Sueno, T. Toyama, M. Watanabe, and I. Yamane. Observation of the Acceleration of a Single Bunch by Using the Induction Device in the KEK Proton Synchrotron. *Phys. Rev. Lett.*, 94:144801–144804, 2005.
31. K. Takayama, Y. Arakida, T. Dixit, T. Iwashita, T. Kono, E. Nakamura, K. Otsuka, Y. Shimosaki, K. Torikai, and M. Wake. Experimental Demonstration of the Induction Synchrotron. *Phys. Rev. Lett.*, 98:054801–054804, 2007.
32. T. Dixit, Y. Shimosaki, and K. Takayama. Adiabatic Damping of the Bunch Length in the Induction Synchrotron. *Nucl. Inst. Meth. A*, 582:294–302, 2007.
33. K. Nakahiro, W. Jiang, N. Shimizu, S. Yoshida, K. Nakahishi, A. Sugiyama, M. Wake, and K. Takayama. Development of High Repetition-Rate Pulse Generator Using Static Induction Thyristors. In *Proceedings of the International Workshop on Recent Progress in Induction Accelerators*, pages 88–90, Tsukuba, Japan, 7–10 Mar. 2006. KEK.